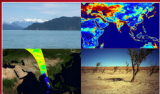# Remote Sensing of the Terrestrial Water Cycle

Venkat Lakshmi

Douglas Alsdorf, Martha Anderson, Sylvain Biancamaria, Michael G. Cosh, Jared Entin,
George J. Huffman, William Kustas, Peter van Oevelen, Thomas H. Painter, Juraj Parajka,
Matthew Rodell, Christoph Rüdiger
Editors

CONTENTS

1

Rain/No-Rain Classification Using Passive Microwave Radiometers

J. Indu[1] and D. Nagesh Kumar[1,2]

1.1. INTRODUCTION

Precipitation is a critical variable driving the atmosphere's general circulation through latent heat release. As such, accurate quantification of the spatiotemporal variability of precipitation is essential for applications involving environmental, atmospheric, water resource, and related science and engineering disciplines. The increased availability of data products from microwave (passive and active) remote sensing has contributed toward our understanding of the spatiotemporal distribution of precipitation by providing near-real-time spatially continuous precipitation estimates at smaller temporal sampling intervals [*Petty,* 1994; *Ferraro,* 1997; *Bauer*, 2001; *Grecu and Anagnostou,* 2001; *Kummerow et al.*, 2001; *Turk et al.*, 2002; *McCollum and Ferraro*, 2003; *Wilheit et al.,* 2003; *Ferraro et al.*, 2005; *Levizzani and Gruber*, 2007]. These include data products from the Special Sensor Microwave Imager (SSM/I) on Defense Meteorological Satellite Program satellites [*Ferraro,* 1997], Advanced Microwave Sounding Unit (AMSU) on National Oceanic and Atmospheric Agency (NOAA) Polar Orbiting environmental satellites [*Ferraro et al.*, 2005], Tropical Rainfall Measuring Mission (TRMM) microwave imager (TMI) and precipitation radar (PR) [*Kummerow et al.*, 2001; *Wang et al.*, 2009], Advanced Microwave Scanning Radiometer-Earth Observing System (AMSR-E) [*Wilheit et al.*, 2003] on National Aeronautics and Space Administration (NASA) and Japan Aerospace and Exploration Agency (JAXA) joint satellites, etc. Along with the widespread acceptance of microwave-based

precipitation products, it has also been recognized that these products contain large uncertainties [*Petty*, 1994; *Smith et al.*, 1998; *Kummerow et al.*, 1998, 2005; *Coppens et al.*, 2000]. Studies quantifying global uncertainty offered by microwave rainfall algorithms show climatologically distinct space/time domains that contribute approximately 25% uncertainty to rainfall product that goes undetected by a microwave radiometer [*Kummerow et al.*, 2005]. Of these, nearly 20% is attributed to changes in cloud morphology and microphysics and 5% to changes in the rain/no-rain thresholds. The purpose of this chapter is to describe the foundations of rain/no-rain classification (RNC) based on passive microwave brightness temperatures, outstanding issues, areas of future research, and a comprehensive review of the existing RNC algorithms, based on the works by *Grody* [1991], *Adler et al.* [1993], *Ferraro et al.* [1998], *Seto et al.* [2005, 2009], *Kida et al.* [2009], and *Kubota et al.* [2007].

The physically based overland rainfall retrieval algorithms incorporate rainfall screening as an integral part, without which the succeeding overland rain retrieval technique gets corrupted easily. From the work by *Grody* [1991], "*the physics of rain detection and screening are every bit as important as those of conversion*." Studies by rainfall intercomparison projects including algorithm intercomparison projects sponsored by the Global Precipitation Climatology Project and NASA WetNet Precipitation Intercomparison Projects conclude that inadequate screening of nonraining pixels complicates the simplest to the most complex of retrieval algorithms.

To date, various approaches exist to detect raining areas within a radiometer footprint. While some of these techniques are easy to implement, some others involve sophisticated programming logic for correct implementation.

[1]*Department of Civil Engineering, Indian Institute of Science, Bangalore, India*

[2]*Centre for Earth Sciences, Indian Institute of Science, Bangalore, India*

Currently, there exist two schools of thoughts for describing rainfall screening methodologies. One approach addresses screening as part of the rainfall retrieval problem. The other approach considers RNC as an essential preprocessing step for proper identification of potential rain measurements before the actual retrieval process. Regardless of which philosophy is followed, typical RNC classification algorithms should accurately identify rainfall signatures over surfaces covered with snow/ice that offer difficulty in uniquely separating rainfall signature from the surface conditions. This implies that an algorithm should either "dynamically" determine nonraining pixels or it should depend on suitable surface masks based upon climatology (e.g., for snow and ice) or geography (e.g., for deserts) [*Ferraro et al.*, 1996]. The organization of this chapter is as follows: Section 1.2. presents a discussion on the fundamental principle of passive microwave data and radiative transfer model. Atmospheric attenuation (i.e., reduction of a signal due to atmospheric gases, hydrometeors) is a critical factor affecting radiometer brightness temperature. Hence, Section 1.3. discusses the complex interactions of atmospheric hydrometeors (like water vapor, ice, precipitation) with different microwave frequencies. Section 1.4. describes the fundamentals of the RNC classification technique and highlights prominent RNC algorithms that are embedded in the Goddard profiling (GPROF), the global satellite mapping (GSMaP) of precipitation, and the Goddard scattering (GSCAT) algorithms. Section 1.5. summarizes various indices used for performance evaluation of a typical RNC classification. Compared to RNC classification over oceans, overland classification offers a myriad of complications as land presents itself as a radiometrically warm background with highly varying surface emissivities [*Spencer et al.*, 1989; *Grody*, 1991; *Adler et al.*, 1994; *Ferraro*, 1997]. The fairly complex atmospheric attenuation in the scattering regime complicates rainfall delineation even further. For these reasons, overland RNC warrants separate attention. There are several open questions that need to be addressed. These have been discussed in Section 1.6. followed by the conclusions in Section 1.7.

1.2. PRINCIPLES OF PASSIVE MICROWAVE SATELLITE MEASUREMENTS

Radiometry is the field of science related to measurement of incoherent electromagnetic radiation. According to thermodynamic principles, all materials (gases, liquids, solids) both emit and absorb incoherent electromagnetic energy. The magnitude of thermal emission I can be expressed as a product of emissivity (ε) and the Planck (blackbody) function $B(T)$ as

$$I_\lambda = \varepsilon_\lambda B_\lambda(T) = [\varepsilon_\lambda(2hc^2\lambda^{-5})]/(e^{hc/\lambda kT} - 1) \quad (1.1)$$

where h is Planck's constant, k is Boltzmann's constant, c is the speed of light, and T is thermal temperature [*Elachi*, 1987]. By approximating the thermal emission from the Planck function using Rayleigh-Jeans formula, the microwave brightness temperature can be conveniently expressed as a linear function of physical temperature and emissivity (ε) as

$$Tb = \varepsilon T_{\text{PhysicalTemperature}}, \quad (1.2)$$

where ε is a complex function of the dielectric constant whose values are quite well known for gases and calm water but not so well understood for the complicated case of rough water and land surfaces [*Elachi*, 1987].

A downward-viewing spaceborne radiometer is built to sense the upwelling electromagnetic energy emanating from the surface, which reaches the top of the atmosphere after attenuation. The brightness temperatures registered by this radiometer depends on absorption and scattering properties of atmosphere and background emissivity, which vary with frequency and polarization. The intensity of brightness temperature (T_b) incident on a spaceborne microwave radiometer (directed toward Earth), indicates radiation received by the spaceborne antenna from regions of space, which are defined by the antenna pattern. "*The antenna pattern is usually strongly peaked along its beam axis. And when pointing towards the ground, its spatial resolution or footprint size is defined by the angular region over which the antenna power pattern is less than 3 dB down from its value at beam center*" [*Njoku*, 1982]. The total noise power resulting from the thermal radiation incident on the antenna, also known as "antenna temperature" is expressed as a function of the antenna gain pattern [$G(\theta, \phi)$] and the brightness temperature distribution incident [TB(θ, ϕ)] as

$$T_a = \frac{1}{4\Pi} \iint\limits_{4\Pi} T_b(\theta, \phi) G(\theta, \phi) \, d\Omega. \quad (1.3)$$

As shown in Figure 1.1, the distribution of T_b is composed of self-emitted radiation from land/sea, upward emission from the atmosphere, and downward atmospheric emission that is rescattered by the surface toward the antenna coupled with atmospheric attenuation. Therefore, an interpretation of T_b will essentially reveal the physical properties of the media that produce them. Knowing the atmosphere, surface environmental parameters, and radiometer characteristics, radiative transfer models (RTMs) can be used to normalize the measured T_b to a common reference for comparison. This implies that RTMs can interpret T_b from radiometers with different characteristics having different viewing geometries (incidence angles) and operating at different frequencies [*Chandrasekhar,*

Figure 1.1 Spaceborne radiometer observing the ocean at a nadir angle θ.

1960; *Volchok and Chernyak*, 1968; *Paris,* 1971; *Snider and Westwater,* 1972; *Fraser,* 1975; *Savage,* 1976; *Wilheit et al.*, 1977]. Several factors contribute to the quantitative accuracy of RTMs such as the realism in specifying hydrometeor shape, size, and phases encountered in real rain clouds, knowledge of vertical hydrometeor profiles, and proper generation of local radiative interaction properties (like single scatter albedo, extinction coefficient, etc.).

The general problem of radiative transfer was solved by *Chandrasekhar* [1960] and further extended for microwaves in a cloudy atmosphere by *Volchok and Chernyak* [1968], *Paris* [1971], *Snider and Westwater* [1972], *Fraser* [1975], *Savage* [1976], and *Wilheit et al*. [1977]. For a medium in thermodynamic equilibrium, the change in microwave intensity I_λ over a distance ds in the direction (θ,ϕ) is given by the expression:

$$\frac{dI_\lambda}{ds} = -\left(k_{ab} + k_{sc}\right)I_\lambda + k_{ab}B_\lambda + \frac{k_{sc}}{4\Pi}$$
$$\int_0^{2\Pi}\int_0^{\Pi} P_\lambda'\left(\theta_s,\phi_s,\theta,\phi\right)I_\lambda\left(\theta_s,\phi_s\right)\sin\theta_s\,d\theta_s\,d\phi_s, \quad (1.4)$$

where, $P_\lambda'\left(\theta_s,\phi_s,\theta,\phi\right)$ is an inverse scattering phase function that describes the relative contribution of each polar angle θ_s and each azimuthal angle ϕ_s to the energy

scattered in the direction (θ,ϕ); and k_{ab}, k_{sc} denote the absorption and scattering coefficients, respectively. In other words, the gradient of I_λ along s is determined by the balance of energy lost by absorption and by scattering out of the direction of I and energy gained by thermal emission and by scattering into the direction of I. The literature presents several solutions for RTM based on the assumptions of Marshall Palmer drop size distribution, horizontally homogeneous atmosphere in thermal equilibrium [*Savage et al.*, 1995; *Lovejoy and Austin,* 1980]. Generally, forward radiative transfer equations found in the literature are either scalar or vector models. While the scalar model solves radiative transfer equations with a single Stokes' parameter and considers only the polarization effects caused by the surface, vector models consider polarization effects caused by both surface and hydrometeors. Vector models consider four Stokes' parameters, which make the calculations complex and difficult to implement. Hence, vector models require comparatively larger amount of computational time when compared with scalar models. These will not be discussed in this chapter. Comprehensive details regarding microwave radiative transfer are given in *Liou* [1980] and *Janssen* [1993].

Uncertainty in effectively interpreting microwave T_b stems from several factors, like antenna pattern, deviation of spacecraft attitude parameters (roll, pitch, yaw),

alteration of land surface emissivity during rainfall, nonhomogeneity of land surfaces that results in high and variable surface emissivity, atmospheric attenuation, etc. Attenuation results from the complex interaction of electromagnetic waves with ice, water vapor, oxygen, and other precipitation sized hydrometeors aloft, which can be liquid and/or solid and which may precipitate to surface as rainfall or snowfall depending on the temperature in the subcloud layer. As atmospheric attenuation complicates detection of rainfall signature within T_b, knowledge regarding the sources and sinks of microwave radiation within the atmosphere is crucial to fully understand these uncertainties.

1.3. ATMOSPHERIC ATTENUATION OF MICROWAVES

With the advent of microwave radiometers on board satellites like Defence Meteorological Satellite Program (DMSP), TRMM, Global Precipitation Mission (GPM), Megha Tropiques (MT), etc., microwave rainfall products have become an indispensable source for precipitation information and for real-time applications in flood forecasting. A choice of frequency channels on board these satellites are made based on the geophysical parameter to be studied and its sensitivity to major atmospheric constituents. Several studies have examined the response of microwave frequency channels due to precipitation-sized particles in the atmosphere [*Weinman and Guetter,* 1977; *Spencer*, 1986; *Wu and Weinman*, 1984]. Works have also been conducted to estimate sensitivity of T_b to variations in atmospheric and precipitation parameters using cloud radiative models such as those by *Weinman and Guetter* [1977], *Wilheit et al.* [1982], *Wu and Weinman* [1984], *Szejwach et al.* [1986], *Olson* [1987], and *Kummerow and Weinman* [1988]. This section describes the field of spectroscopy, an age-old science explained by quantum mechanics during the first half of the twentieth century involving the study of absorption and emission by gases. The five possible ways in which radiation interacts with atmospheric gases are ionization-dissociation interaction, electronic transition, vibrational transition, rotational transition, and forbidden transition [*Kidder and Vonder Haar*, 1995]. Among these, vibrational and rotational transitions are important for satellite meteorology as they occur mostly in the infrared and microwave portion of the electromagnetic spectrum. Some of the prominent sources causing atmospheric attenuation of microwaves are discussed below.

1.3.1. Absorption by Gaseous Atmosphere

An extensive study of microwave absorption of atmospheric gases (both theoretically and experimentally) shows that, emission/absorption in gaseous atmosphere is dominated by the presence of water vapor and oxygen [*Waters*, 1976; *Ulaby and Stiles*, 1981]. Absorption characteristics of these gases are summarized by *Staelin* [1969], *Paris* [1971], *Derr* [1972], *Waters* [1976], and *Fraser* [1975]. Microwaves undergo resonant absorption and emission at certain frequencies due to the quantum energy states of the water vapor/oxygen molecules. Within microwave spectrum, these molecules are subjected to rotational transition wherein a molecule changes rotational energy states. This causes a peak in T_b measured by a radiometer. The magnitude of increase in T_b depends on the total number of water vapor/oxygen molecules along the propagation path through the atmosphere. At higher altitudes there is a decrease in the number of water vapor/oxygen molecules per unit volume. This in turn reduces the bandwidth of water vapor/oxygen emission (absorption) leading to an increase in absorption at the peak of resonance. The rotational lines of water and oxygen are "pressure broadened" in the atmosphere owing to the presence of other gases; there is also a slight dependence on temperature [*Kidder and Vonder Haar*, 1995]. Water vapor has a weak absorption line at 22.235 GHz and a strong line at 183 GHz. All sensors currently used for precipitation make a measurement near 22.235 GHz like TMI at 21.3 GHz and AMSR at 23.8 GHz. Oxygen has two major peaks, one near 60 GHz and another at 118.75 GHz. More details regarding the absorption characteristics of atmospheric water vapor and oxygen can be obtained from *Paris* [1971] and *Fraser* [1975].

1.3.2. Cloud Liquid Water

In an atmosphere with cloud particles, the prominent sources and sinks of microwave energy are local emission and absorption. In the scattering regime, cloud droplets interact weakly with microwave radiation. As the cloud liquid water particles are usually less than 100 μm in diameter, much smaller than the wavelength of radiation, for this Rayleigh region, the scattering effect is negligible. Generally, for the Rayleigh regime, the effect of cloud particles on microwave radiation depends on liquid water content, cloud temperature, and wavelength of radiation. When microwave radiation interacts with rain clouds, the phenomenon is similar to an ensemble of drops with no coherence from drop to drop in the phase of scattered light. Within a rain volume, the usual practice is to assume the raindrops to be randomly distributed. Once we calculate the scattering and absorption for a single drop of spherical dielectric, it is possible by integration to determine corresponding coefficients for a rain cloud that is an ensemble of drops. The particle sizes of raindrops within a rain-bearing cloud are usually described by a continuous function known as drop size distribution (DSD). This function is responsible for defining the concentration of rain particles per unit volume per unit increment of the drop radius.

Studies by *Fraser* [1975] estimated the single-scatter albedo as a function of wavelength for DSD representing very thin fair weather cumulus and very dense cumulonimbus clouds. Generally, for cumulus clouds, scattering remains negligible at all wavelengths. For cumulonimbus clouds raining at 150 mm/h, scattering will be small only for all values of wavelength >~3 cm. Studies by *Lovejoy and Austin* [1980] concluded that scattering can be neglected for all clouds if wavelength is >0.5 cm, and for rain rate <10 mm/h if wavelength is >1 cm [*Stepanenko*, 1968; *Wilheit et al.*, 1977]. A complete and published summary of extinction, scattering, and absorption coefficients and scattering phase functions is available in *Savage* [1978]. Savage approximated the scattering phase functions by Legendre polynomials, and expressed the Legendre coefficients (for the phase function) and extinction, scattering, and absorption coefficients as power law relations in liquid water content [*Barrett and Martin*, 1981]. *Lovejoy and Austin* [1980] assessed the relative contribution of cloud droplets and raindrops to total cloud layer absorption and came out with the conclusions that at rain rates = 10 mm/h, cloud absorption was 30–40% as large as rain absorption. This conclusion was consistent with the observations by *Gorelik et al.* [1971]. In 1976, Savage stated that addition of a non-scattering cloud layer above the rain layer counteracted scattering and resulted in T_b increase by an amount proportional to the cloud layer thickness. It must be noted that as cloud droplets, water vapor, and oxygen all absorb (but do not scatter) microwave radiation, they have the potential to confuse precipitation estimates based on absorption [*Barrett and Martin*, 1981]. Authoritative treatment of this subject may be found in *Gunn and East* [1954], *Shifrin and Chernyak* [1968], *Paris* [1971], *Schwiesow* [1972], *Hansen and Travis* [1974], *Savage* [1976], and *Fraser* [1975].

1.3.3. Surface Emission

In the microwave spectrum, an emitting surface must be considered as a gray body so that its emissivity value stays lower than unity. For homogeneous land surfaces, the variability in microwave radiances depends on surface skin temperature and surface emissivity, while the variability for open water bodies is attributed to the atmospheric constituents such as columnar water vapor, temperature profiles, and presence of cloud liquid water. Unlike the oceans, it is very difficult to model land surface properties in the microwave spectrum due to the spatiotemporal variations of soil features like roughness, vegetation cover, and moisture content. The response of different surface types on the temperature and humidity retrievals has been quantified by *English* [1999]; in these studies microwave emission errors for different continental surfaces were evaluated by using a mathematical technique to potentially extend the low-altitude sounding information over solid surfaces. Microwave land surface emissivity for various surface conditions on a global scale was attempted by *Prigent et al.* [1998], *Weng et al.* [2001], and *Pellerin et al.* [2003].

Different surfaces contribute varying amounts of emission to a microwave radiometer footprint. Figure 1.2 shows the T_b variations for different microwave frequency channels over land and ocean surfaces [*Ferraro et al.* 1998].
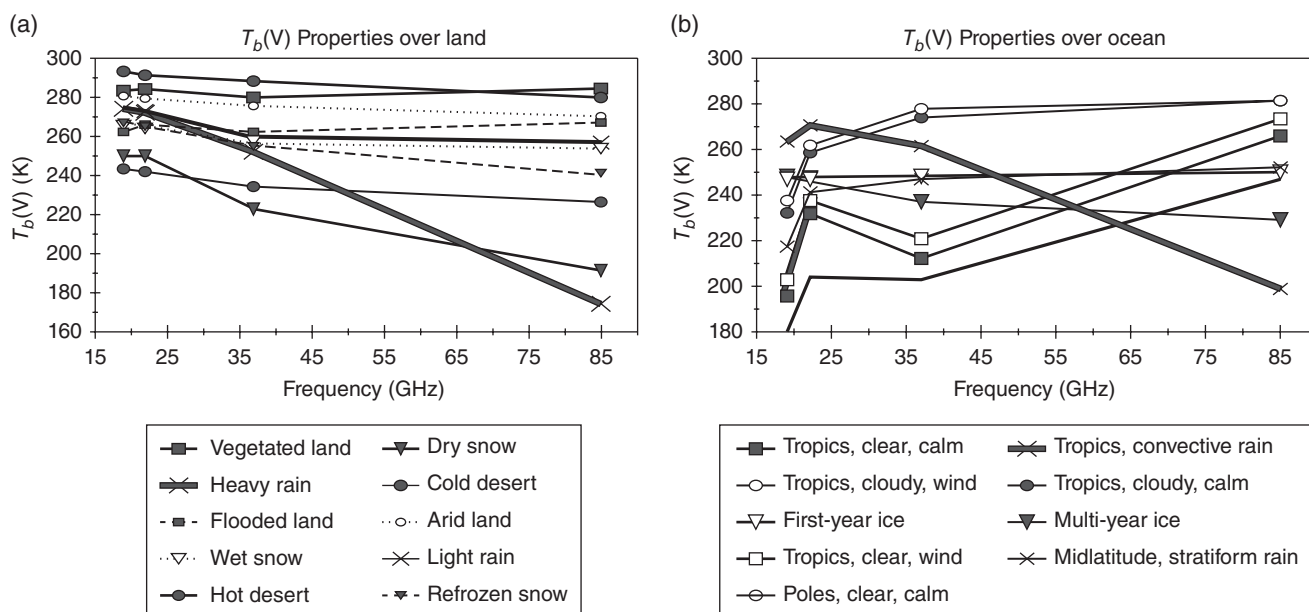
Figure 1.2 Emissivity characteristics of various surface types represented by T_b as a function of frequency (a) over land and (b) over ocean [*Ferraro et al.,* 1998].

Oceans provide a stable and uniformly "cold" background for a radiometer, emphasizing more the extinction of upwelling radiation by atmospheric constituents. Emissivity of sea surface is dependent on the dielectric properties of seawater through the Fresnel equation. Studies were conducted to predict the dielectric constant of seawater with an aim to improve the retrieval of atmospheric parameters [*Klein and Swift*, 1977]. Over snow-covered soil, the emissivity values depend on the dielectric constant of frozen soil (~3), thickness, water equivalent, and liquid water distribution. If snow is dry, T_b decreases with an increase in snow water equivalent. In the case of wet snow, even a small increase in the amount of liquid water causes T_b to rise due to volume scattering. The dependence of snow on T_b is more prominent at microwave frequencies >8–12 GHz. In the presence of vegetation, microwave radiation gets emitted, absorbed, and scattered with the radiative properties mostly controlled by the vegetation density, dielectric properties, and relative size of vegetation components with respect to wavelength. Increasing vegetation density increases the emissivity in horizontal polarization and reduces the emissivity polarization difference [*Prigent et al.*, 1997]. In effect, the presence of vegetation reduces the radiometric sensitivity to soil moisture. Studies have developed computational schemes to improve the mathematical description of surface emissivity for several land types: bare soil, vegetation canopy, and snow-covered terrain [*Shi et al.*, 2002; *Ferrazoli et al.,* 2000; *Fung,* 1994].

Theoretical models for microwave emission from soils have been presented by many studies [*Njoku and Kong,* 1977; *Wilheit,* 1978; *Burke et al.,* 1979; *England,* 1976] by considering emission from soil for a range of moisture and temperature profiles. At low microwave frequencies, T_b is strongly affected by soil moisture content. This strong dependence is owing to the comparatively high dielectric constant of water (~80) compared to that of dry soil. The dielectric constant of wet soil can reach 20 or more, resulting in an emissivity change at 1.4 GHz from about 0.95 for dry soil to 0.6 for wet soils. Despite a strong sensitivity of the emissivity on soil moisture, microwave remote sensing of soil moisture from space is complicated due to highly varying surface roughness and vegetation cover, which is aggravated by the presence of mixed surfaces within satellite field of view (FOV). To summarize, varying emissivity values from spatiotemporal variations of land surface types can deeply affect radiometer observations, often leading to rainfall retrieval errors.

1.3.4. Ice

Ice particle shapes are crucial in scattering regimes, as they significantly affect the emerging radiance field [*Mugnai and Wiscombe,* 1986; *Bohren,* 1986]. Crystals of ice exhibit a large variety of shapes and modes depending on atmospheric temperature and humidity conditions. If we simplify the domain of shapes that the ice nucleation process can create, they can be considered as columns and plates. The usual practice is to adopt a Marshall-Palmer size distribution for ice particle sizes in all theoretical treatments.

Sensitivity of T_b values to the integrated mass of ice/rain depends on frequency, until the optical depth reaches the saturation level [*Evans et al.*, 1995]. *Fulton and Heymsfield* [1991] studied the response of T_b (18, 37, 92, 183 GHz) to hydrometeors due to intense convection and suggested that even the lowest microwave frequency channel (18 GHz) is significantly obscured by deep convective ice mass. Generally, with an increase in microwave frequency (>60 GHz), scattering signatures become more pronounced and a dramatic increase is observed in volume scattering (k_s), absorption coefficients (k_a), and single-scatter albedo. This is because the aging of ice results in internal voids that tend to scatter microwave radiation. And, an increase in microwave frequencies is accompanied by an increase in the scattering cross section of inhomogeneities, thereby causing a decrease in radiation emanating from them. Thus, at higher frequencies, scattering dominates with microwave radiation acting relatively transparently to the rain below freezing level. In satellite meteorology, the high single-scatter albedo produced by ice is crucial, as it heavily depresses high-frequency microwave channels. Ice has much smaller absorption coefficients than water that result in high albedos at all SSM/I frequencies. A single scatter albedo approaching unity indicates that any thermal radiation upwelling from below an ice layer that is attenuated by the ice will be scattered out of the radiometer's field of view, with very little ice-emitted radiation to replace it [*Spencer et al.*, 1989]. When the scattering coefficient is large, and since there is very little (2.7 K) downwelling radiation from cosmic background, very low values of T_b will be recorded at 85.5 GHz frequency. This extremely low T_b observed is usually attributed to convective rainfall. Due to the high sensitivity of 85.5 GHz frequency to frozen ice, RNC algorithms for land regions are essentially based on ice scattering at this frequency. Studies have also been conducted by *Anagnostou and Kummerow* [1997] that suggest that as T_b at 85.5 GHz (V) frequency is more variable in raining than in nonraining area, studies of rainfall screening can utilize even the standard deviation of T_b at 85.5 GHz (V) frequency in a 5 × 5 pixel window [*Biscaro and Morales*, 2007].

1.3.5. Precipitation

At microwave wavelengths, precipitation-sized drops interact strongly with microwave radiation [*Kidder and Vonder Haar*, 1995]. Interaction of electromagnetic (EM)

waves with a spherical dielectric causes scattering (redirecting) or absorption (conversion to mechanical energy) of radiation depending on the size of precipitation particles [*Barrett and Martin*, 1981]. One of the earlier studies by *Mie* [1908] introduced the general mathematical solution for scattering and absorption of EM waves by a dielectric sphere of arbitrary radius. Later on, this was applied to the context of rain by *Gunn and East* [1954]. The expressions for Mie efficiency factors are given by

$$Q_{ex}\left(n_c,\lambda\right)=\frac{\sigma_{ex}}{\Pi r^2}, \tag{1.5}$$

$$Q_{sc}\left(n_c,\lambda\right)=\frac{\sigma_{sc}}{\Pi r^2}. \tag{1.6}$$

In equations (1.5) and (1.6), r denotes the radius of the rain drop, λ stands for the wavelength, and n_c represents the complex index of refraction; Q_{ex} and Q_{sc} refer to the Mie efficiency factors of extinction coefficient and scattering coefficient for a single drop. The symbols σ_{ex} and σ_{sc} represent the effective cross sections for extinction and scattering.

*Frase*r [1975] has calculated the Mie efficiency factors for extinction and scattering and the Rayleigh extinction coefficient for a range of drop sizes [*Barrett and Martin*, 1981]. If we consider a single raindrop particle whose size is much smaller than the wavelength of EM waves, Rayleigh approximation to the exact Mie expression applies. The absorption cross section will then be proportional to the cube of particle diameter and hence proportional to the volume and mass of the raindrop while scattering cross section will be negligible. When cloud drops coalesce into raindrops with dimensions comparable to microwave wavelengths, absorption per unit mass increases and scattering can no longer be ignored. Based on the theoretical calculations by *Savage* [1976], rain rates of even a few millimeters per hour cause depression (below 260 K) in T_b for microwave frequencies close to 100 GHz. Studies by *Kidder and Vonder Haar* [1977] used T_b threshold values to discriminate raining from nonraining pixels. Although attempts to use measurements at 37 GHz for land regions [*Weinman and Guetter*, 1977; *Spencer et al.*, 1983; *Spencer*, 1986] met with partial success, mainly in cases of heavier convective rainfall, more reliable microwave rainfall monitoring was made possible only after the launch of SSM/I (1987) [*Barrett et al.,*1988; *Spencer et al.*, 1989]. *Spencer et al.* [1989] calculated the scattering and absorption properties of rain for the three main wavelengths (19.35, 37, 85.5 GHz) that have been used to measure precipitation (Figure 1.3). Their study came out with the conclusions that liquid drops both absorb and scatter microwaves of which absorption dominates [*Kidder and Vonder Haar*, 1995], especially in the frequency range below 22 GHz. This implies that, in this frequency range,
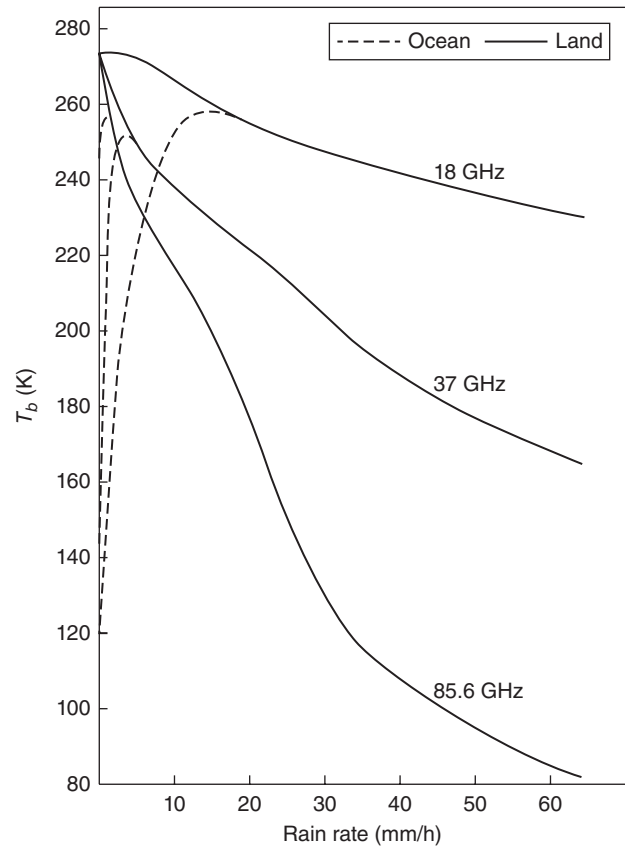
Figure 1.3 Relationship of T_b rain rate at 18, 37, and 85.6 GHz. [Reprinted from radiative transfer modeling of *Wu and Weinman*, 1984.]

scattering does not occur and ice particles above rain are nearly transparent. Another prominent result of their study is that with an increasing rain rate, scattering and absorption both increase with microwave frequencies.

1.4. RAIN/NO-RAIN CLASSIFICATION METHODS

An ideal approach toward understanding the fundamentals of RNC classification is based on the emissivity characteristics of background surface. RNC algorithms follow different principles when the underlying surface is land or ocean. Ocean surfaces, which appear "cold" to a radiometer operating in the microwave region, offer good contrast for the detection of rain drops, which appear radiometrically warm. As this phenomenon utilizes the strong physical relationship between low-frequency (6–37 GHz) T_b and liquid rainfall, overocean techniques are essentially emission based. Land, however, offers a radiometrically warm background, which tends to hide emission from raindrops. Overland RNC techniques solely rely on ice scattering at a high-frequency (85 GHz) microwave channel and are ambiguous in nature [*Wilheit*,

1986; *Spencer et al.,* 1989; *Grody*, 1991; *Adler et al.,* 1993; *Ferraro and Marks*, 1995; *Lin and Hou,* 2008; *Wang et al.,* 2009; *Gopalan et al.,* 2010]. This is mainly due to the highly varying emissivity from the land surface background that clutters rainfall signature. The complicated nature of high-frequency microwave scattering with ice crystals adds to the uncertainty, thereby rendering the use of radiative transfer models extremely difficult. It should be noted that the microwave frequencies are utilized to retrieve several geophysical parameters over ocean; for example, 6.8 and 37 GHz are used for wind speed retrieval [*Wentz*, 1983], 7 GHz is used for retrieving sea surface temperature [*Chelton and Freilich*, 2005], and so forth.

Some of the first rainfall screening studies were by *Ferraro* et al. [1986] and *Wentz* and Cavalieri [1995]. They proposed using multiple channels to identify a rainfall signature from radiometer-received T_b. Their study, involved an intensive analysis of Scanning Multichannel Microwave Radiometer (SMMR) passes over central North America on 20 January, 1979. The study region was chosen to represent a wide variety of surface and atmospheric features ranging from harsh winter conditions and deep snow cover in the northern latitudes to heavy convective rains.

Based on the criteria of spatial resolution and sensitivity to surface parameters, differences between 18 and 37 GHz channels were selected as the optimum channel combination for rain/no-rain discrimination. Their study observed that the presence of clouds and precipitation led to an increase in T_b. *Ferraro et al.* [1994] expanded on these ideas and developed a set of geographical screens for land, ocean, semiarid land, coastlines, and sea ice. Using SSM/I data over ocean surfaces, *Wentz and Cavalieri* [1995] proposed the no-rain algorithm based on the fundamental principles of radiative transfer and explicitly showed the physical relationships between the input (T_b) and the output (wind speed, columnar water vapor, columnar cloud liquid water, rain rate, and effective radiating temperature for upwelling radiation). Later on, this algorithm was extended to include the effects of rainfall. Comprehensive details can be found in *Wentz* [1997]. The screening methodology that has evolved continuously throughout the years is the Grody-Ferraro screening methodology (discussed in Section 1.4.1). This is currently built in to the GPROF algorithm [*Kummerow et al.,* 2001]. Various versions of GPROF have been applied in SSM/I, TMI, and AMSR-E missions [*McCollum and Ferraro*, 2003; *Wang and Wolff*, 2010]. The purpose of this section is to describe the major indices used for demarcating the rainfall signature within a microwave FOV, through which we discuss some of the prominent RNC algorithms adopted for land, ocean, and coastlines, using data from satellites like SSM/I, TRMM, etc.

1.4.1. Scattering Index

The technique of using a scattering index (SI) to delineate raining pixels originated from the studies by *Grody* [1991]. Initially, the idea was proposed to create geographical masks for eliminating T_b cluttering due to desert sand and ice-capped land surfaces. This was essential, as uncertainty in detecting scattering caused by desert/ice-capped surfaces led to false estimates of rainfall over these regions. RNC algorithms based on SI by *Grody* [1991] largely relied on regression relationships of microwave low-frequency channels, especially the 19 and 22 GHz. Vertical polarization measurements were preferred, as they resulted in smaller aliasing effects in the presence of mixed boundaries (e.g., coastlines). *Adler et al*. [1993] devised a global empirical relation for SSM/I to calculate the estimated value of T_b at 85 GHz (V) under nonrainy conditions ($T_{b, Estimated}$), using a fixed quantity of 243 K. Later on *Ferraro et al*. [1994] and *Ferraro and Marks* [1995] introduced the concept of using low-frequency channel combinations (10–37 GHz) to represent $T_{b, Estimated}$. Since the introduction of Grody-Ferraro screening methodology [*Ferraro et al*., 1986, 1998; *Grody,* 1991], it has been the most applied technique for use in microwave land precipitation algorithms. The key idea in this technique is that radiation emitted from land surfaces is affected by ice particles and raindrops at high frequency 85 GHz T_b. Calculation of $T_{b, Estimated}$ involves simulation of 85 GHz T_b values for clear sky conditions (i.e., nonscattering condition). The difference between $T_{b, Estimated}$ and the observed 85 GHz T_b ($T_{b, Observed}$) gave a measure quantifying the degree of scattering by ice particles and raindrops, wherein the rain rate is proportional to the amount of scattering. As rainfall SI models offered an indirect and nonunique relation that varied from region to region, empirical relationships were largely employed between precipitation and SI to map rainfall over land surfaces [*Spencer et al*., 1989*; Kidd and Barrett*, 1990; *Conner and Petty*, 1998; *Adler et al*., 1994; *Dinku and Anagnostou* 2005].

As experience with SI-based studies grew, it became increasingly clear that a new suite of algorithms was necessary that efficiently modeled the value of $T_{b, Estimated}$ to suit the highly varying emissivity from the background land surface. Results of the ensuing development for overland regions are summarized in Table 1.1. Approaches involved using 85 GHz (H) channel instead of 85 GHz (V) channel to depict $T_{b, Observed}$ [owing to the failure of the first of SSM/I's 85.5 GHz (V) channel T_b] [*Adler et al*., 1994; *Kummerow and Giglio* 1994], using channels of 19 GHz (V) and 22 GHz (V) to represent $TB_{Estimated}$ owing to their increased sensitivity to land surface emissivity. SI-based RNC classification techniques are currently being used for overland RNC classification embedded in

Table 1.1 Prominent scattering index based RNC methods

Sl No:	Algorithm Proposed by	Observed T_b (K)	Estimated T_b (K)	SI Threshold (K)
1.	*Grody* [1991]	85(V)	$450.2 - 0.506 \times T_{b,19V} - 1.874 \times T_{b,22V} + 0.006 \times T_{b,22V}^2$	SI > 10
2.	*Adler et al.* [1994] (GSCAT)	85(H)	251	SI > 4
3.	*Kummerow and Giglio* [1994]	85(H)	$\mathrm{Min}[T_{b,37H}, 265]$	SI > 0
4.	*Ferraro* [1997]	85(V)	$451.9 - 0.44 \times T_{b,19V} - 1.775 \times T_{b,22V} + 0.005 \times T_{b,22V}^2$	SI > 10
5.	*Ferraro* [1997]	37(V)	$62.18 + 0.773 \times T_{b,19V}$	SI > 5
6.	*Kummerow et al.* [2001] (GPROF)	85(V)	$T_{b,22V}$	SI > 8
7.	M1 [*Seto et al.,* 2005]	85(V)	μ	SI > $k_0 \sigma$
8.	M2 [*Seto et al.,* 2005]	85(V)	$a + b \times T_{b,22V}$	SI > $k_0 \sigma_e$

Source: Modified and adapted from *Seto et al.* [2005].

prominent algorithms such as GSCAT and GPROF algorithms, which are discussed in Sections 1.4.3 and 1.4.4.

1.4.2. Polarization-Corrected Temperature

Atmospheric hydrometeors have a depolarizing effect on microwave radiation that is emitted and reflected from a highly polarized surface [*Wu and Weinman*, 1984; *Huang and Liou*, 1983]. Therefore, polarization offers a great deal of information for separating the highly polarized radiances of the ocean from the essentially unpolarized radiances due to precipitation volume scattering [*Weinman and Guetter*, 1977]. *Spencer et al.* [1989] proposed an index comprised of linear combinations of vertical and horizontal polarizations to eliminate contrast between land and water/wet surfaces to yield a precipitation signal whose interpretation does not vary much depending on the background surface. The conceptual diagram of this index, known as polarization-corrected temperature (PCT) is shown in Figure 1.4.

The PCT relates the vertically and horizontally polarized T_b, and *Spencer et al.* [1989] described it as a measure of the distance from the no-scattering line. Earlier studies by *Spencer* [1986] noted that upon addition of nonscattering materials to the atmosphere above a nonraining, oceanic scan spot, the observed T_b will tend to move along the no-scattering line. When scattering materials (e.g., precipitation) gets introduced into the atmosphere, the point moves off the no-scattering line. As scattering lowers the T_b values, observations in which precipitation occurs will essentially fall between the no-scattering line and the no-polarization line. If $T_{b,\mathrm{HCLF}}$ and $T_{b,\mathrm{VCLF}}$ refer to the horizontally and vertically polarized cloud free ocean T_b respectively, $T_{b,\mathrm{H}}$ and $T_{b,\mathrm{V}}$ are the horizontally and vertically polarized T_b that are at least partially affected by any combination of clouds and precipitation, $T_{b,\mathrm{VOLA}}$ and $T_{b,\mathrm{HOLA}}$ are the vertically
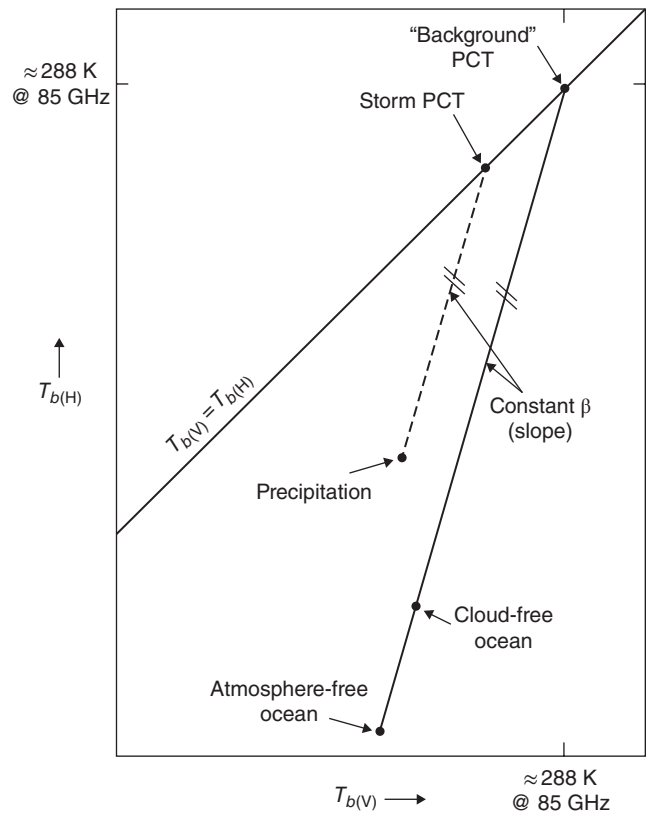
Figure 1.4 Schematic diagram of vertically and horizontally polarized T_b of ocean with and without an overlying atmosphere [*Spencer et al.*, 1989].

and horizontally polarized T_b of the ocean with no overlying atmosphere, then the expression for PCT is given by

$$\mathrm{PCT} = \frac{\beta T_{b,\mathrm{H}} - T_{b,\mathrm{V}}}{\beta - 1}, \qquad (1.7)$$

where

$$\beta = \frac{T_{b,\text{VCLF}} - T_{b,\text{VOLA}}}{T_{b,\text{HCLF}} - T_{b,\text{HOLA}}}. \qquad (1.8)$$

Calculation of PCT at any frequency requires a nearly constant value of β. Experiments using SSM/I observations of global cloud-free oceanic areas show that to obtain a physically meaningful value of PCT (between 275 and 290 K) the value of β should be 0.45. Absolute accuracy for β is not as important as keeping it constant in all subsequent calculations. Equation 1.7 for PCT can be rewritten as

$$PCT = 1.818T_{b,v} - 0.818T_{b,h} \qquad (1.9)$$

PCT values using 85.5 GHz frequency channels will generally be lower than the background PCT, although its T_b depression will be much less than that due to the strong volume scattering effects of precipitation. Hence, this property of 85.5 GHz PCT is employed to detect cloud liquid water. Studies by *Mugnai et al.* [1993] using numerical model simulations demonstrated that 85 GHz signals represent emissions from upper-level liquid and ice scattering in the upper reaches of tall precipitation clouds. Therefore, PCT using 85.5 GHz channel is sensitive to precipitation top height for tall convection and surface rainfall for moderate convection. A modified relation for PCT was proposed by *Kidd and Barret* [1990] using SSM/I's 85.5 GHz channels as the basis for estimation of precipitation over both land and water. PCT is currently being used for RNC classification and the succeeding rainfall retrieval oceans and coastlines in the algorithm of the GSMaP, which is discussed in Section 1.4.4

1.4.3. Goddard Scattering Algorithm

The Goddard scattering algorithm (GSCAT) was first proposed by *Adler et al.* [1993]. Their study detected the existence of rainfall signature using an empirical logic tree applied to multiple channels. The algorithm relied on frequencies of 86 and 37 GHz (both in the horizontal polarization) to eliminate nonraining areas. This technique worked well over ocean and land areas but suffered from the inability to detect rain from clouds below the freezing level. Efforts were undertaken to modify the GSCAT RNC algorithm by including geographical screens (for deserts and snow-covered surfaces) similar to the work by *Grody* [1991]. *Adler et al.* [1994] modified this algorithm and included better quality control and use of lower frequency channels to differentiate cold surface and desert from precipitation. This differentiation was

essential when rainfall retrieval is to be made globally. *Adler et al.* [1994] and *Kummerow and Giglio* [1994] created GSCAT2, which used 85 GHz (H) instead of 85 GHz (V), to represent the value of $T_{b,Observed}$ and a constant value (251 K) for $T_{b,\ Estimated}$ without using any regression equations such as *Grody* [1991]. It was developed using channel information from SSM/I sensors. The methodology employed several checks, including the existence of cold ocean, coastline, desert, ice-covered regions, and ambiguous cold surface possible precipitation checks. These checks prevented surface effects that might lead to false identification of rain regions. GSCAT-2 proved to perform successfully in the SSM/I era to demarcate rain/no-rain regions, but not without some false rain identifications. The overall procedure for identifying raining pixels was not all that dissimilar from the scattering index by *Grody* [1991]. In an intercomparison study involving seven microwave techniques over Japan, *Lee et al.* [1991] showed that the GSCAT had the highest correlation with the Grody scheme during the convective regime in July–August 1989. The scattering signatures in GSCAT were used to retrieve rain intensity in proportion to the amount of scattering by ice and graupel aloft based on radiative transfer calculations applied to numerical cloud model results.

1.4.4. Goddard Profiling Algorithm

The GPROF algorithm is considered the established algorithm framework for microwave rainfall products from TRMM (launched in November 1997), Aqua (satellite of AMSR-E launched in May 2002), and included in the initial plans for the proposed Global Precipitation Measurement (GPM) mission (to be launched in 2014). GPROF follows separate sets of algorithms for RNC classification over land, ocean, and coastlines. Various versions of GPROF screening methodology have been implemented in SSM/I, TMI, and AMSR-E missions with an improved version to be applied in GPM mission [*McCollum and Ferraro,* 2003; *Wang et al.*, 2009; *Gopalan et al.,* 2010].

1.4.4.1. RNC Over Land

The RNC classification algorithm of GPROF for land regions [*Kummerow et al.*, 2001] assumes that T_b at 21.3 GHz (V) represents the nonscattering portion of T_b from 85 GHz (V). A scattering index threshold of 8 K is fixed to judge rainfall signature from a pixel/footprint. All pixels that exceed this threshold were identified as "possible rain" and were then processed using the full Bayesian algorithm to quantify the rain rate, which could be zero or nonzero. GPROF version 4 used the screening methodology of GSCAT 2 [*Adler et al.*, 1994]. Version 5 of GPROF [*Petty* 1994] employed polarization-based emission and

scattering indices that could isolate signal coming from rain clouds with the background variability.

1.4.4.2. RNC Over Oceans

Over oceans, the predictable ocean surface emissivity offers contrast to the signals emanating from liquid hydrometeors over the range of microwave frequencies. Yet, the RNC detection technique of TRMM TMI usually fails over oceans to detect shallow rain observed by PR owing to the small scale of shallow rain when compared with the resolution of channels used in the emission-based algorithm. As clouds are optically thick at 85 GHz, it becomes very difficult to use the emission-based algorithm to detect shallow rains. Owing to the contrast between atmospheric liquid and low emissivity ocean surface, screening rainfall pixels over oceans relies on estimation of the liquid water path (LWP). The screening of GPROF over the ocean consists of two processes: checking the LWP and screening out clear ocean pixels and ice surface pixels. The flowchart for GPROF method over the ocean is shown in Figure 1.5.

In the first process, based on the study of *Karstens et al.* [1994], the LWP is checked using TMI low-resolution channels of 22 GHz (V) and 37 GHz (V) using the relation

$$LWP = 0.39 \log\left(285 - T_{b,22V}\right) - 1.40 \log\left(285 - T_{b,37V}\right) + 4.29.$$ (1.9)

All the footprints having LWP values less than the maximum LWP was classified under "no rain," where the value of maximum LWP (kg /m^2) is based on the following relation:

$$LWP\_max = 0.25*\left(\frac{FLH}{4000}\right).$$ (1.10)

Here the value of freezing level height (FLH) is derived from the work by *Wilheit et al.* [1991] and the values of 0.25 and 4000 represent the liquid water content and a typical FLH [*Wilheit et al.*, 1991].

The second process was based on the GSCAT algorithm [*Adler et al.*, 1994], which employed three checks. The first check employed threshold values for T_b from 22 GHz (V) and 85 GHz (H) channels to identify the target pixel as "possibly rain." This check was originally used to screen ice surfaces and "possible rain," but in the GPROF version 6 algorithm, this was utilized to detect rainfall signature. The second check aimed to distinguish ice surfaces from "rain" using T_b at 22 GHz (V). The third check was to identify clear ocean using T_b at 37 GHz (H) and 85 GHz (H). If the target pixel was not identified as ice surface/clear ocean by these checks, it was flagged as "possible rain." After the screening process, the footprints identified as "possible rain" are processed using the Bayesian algorithm to quantify rain rate.

Figure 1.5 Flowchart for RNC method of GPROF over ocean [*Kida et al., 2009*].

1.4.4.3. RNC Over Coasts

Rain identification over land or water involves checks for snow/desert surfaces, which tend to depress the high-frequency microwave channels. Coastlines are much more difficult as, for either water or land surfaces, adding the opposite surface into the footprint will have the same effect as rainfall. Over land, adding surface water to the footprint will reduce the T_b's, as does scattering caused by rain, and adding land to a water footprint will increase T_b's, similarly to rain over water, resulting in emission [*McCollum and Ferraro*, 2005]. Over coasts, microwave footprint is a combination of radiometrically warm land surface and cold ocean surface. One of the very first RNC algorithms developed for coasts was using SSM/I channels by *Adler et al.* [1994]. They proposed a complex decision tree method as shown in Figure 1.6, to isolate rainfall signature without using the SI method by *Grody* [1991]. More details about this method are available in *Huffman and Adler* [1993], which will hereinafter be referred to as HA93. The HA93 algorithm was implemented in GPROF and has remained in use in successive GPROF versions [*Wilheit et al.*, 2003].

Bennartz [1999] provided a technique to account for the coastline complexity, which involved use of effective antenna pattern function and scan geometry of the microwave instrument and high-resolution land-water mask to analyze the fraction of land versus water within each radiometer footprint. The study represented the atmospheric contribution from rain assuming a constant land T_b, while the land versus water fraction was used to weight the relative contribution of land-ocean surfaces to background signal. This technique was implemented to retrieve column water vapor for noncloud conditions using SSM/I data for the Baltic Sea region of western Europe. The study concluded that satellite navigation uncertainty created a dominant source of error. The assumption of a constant value to represent T_b from highly varying land surfaces fails in raining situations, for which cases the method of *Bennartz* [1999] cannot be implemented. The land surface emissivities have not yet been incorporated in the land component of GPROF rainfall algorithms. And, use of a straight cutoff for T_b values also cannot be implemented over coasts as water within the footprint reduces the high-frequency

Figure 1.6 Decision tree for demarcating rainfall over coasts (HA93) [*McCollum and Ferraro*, 2005].

T_b's. As a result, combination of several criteria were examined to classify a footprint as having "no rain," "possibly rain," or "ambiguous." The criteria were mostly determined from the studies of *Grody* [1991] and *Adler et al*. [1993].

The HA93 decision tree method for RNC classification of coastline is summarized in figure 1.6. In this figure, the "clear coast check" by *Adler et al*. [1993] involves the following checks for T_b from 85 GHz (H) and 37 GHz (H):

$$\sigma\left(T_{b,85\mathrm{H}}\right) > 10K, \tag{1.11}$$

$$\rho\left(T_{b,37\mathrm{H}}, T_{b,85\mathrm{H}}\right) > 0.5, \tag{1.12}$$

$$\text{Slope} < 1.2, \tag{1.13}$$

where

$$\text{Slope} = \rho\left(T_{b,37\mathrm{H}}, T_{b,85\mathrm{H}}\right)\left[\frac{\sigma\left(T_{b,85\mathrm{H}}\right)}{\sigma\left(T_{b,37\mathrm{H}}\right)}\right],$$

and σ (standard deviation) and ρ (cross correlation) are computed on a 5×5 footprint array centered on the footprint of interest. This test identifies cases in which low humidity allows the (similar) surface emission signals from $T_{b,37\mathrm{H}}$ and $T_{b,85\mathrm{H}}/T_{b,89\mathrm{H}}$ to dominate the microwave signal [*McCollum and Ferraro*, 2005].

The HA93 algorithm added ambiguous classes for TB combinations for which rainfall rate was retrieved based on the requirement that another scheme be applied to estimate whether the retrieval was useful or an artifact. In case this could not be done, no estimate was made for such footprints in the "ambiguous" class, leaving "holes" in the resulting rainfall map. Footprints that were classified under "possible rain" were required to satisfy a cutoff threshold using higher frequency channels to be flagged as "rain" over land regions. The HA93 algorithm used $T_{b,85\mathrm{H}} < 257\,\mathrm{K}$ criterion to assign a positive rain classification. The study conducted by *McCollum and Ferraro* [2005] using AMSR-E data suggested that a threshold using $T_{b,85\mathrm{H}}$ fails to provide a clear cutoff. The availability of TMI T_b's collocated with TRMM PR rainfall rates enabled choosing cutoff criteria that could efficiently separate raining from nonraining footprints. To summarize, the study by *McCollum and Ferraro* [2005] provided two major improvements to the existing RNC classification algorithm for coasts. The first step was to estimate conditions where positive rain rates should be estimated rather than leaving the areas without estimates as in the previous algorithm. Owing to the high correlation among the various TMI microwave channels, principal component analysis often provides a useful

technique to separate signals of geophysical variables by the creation of mutually orthogonal statistically uncorrelated eigenvectors [*Conner and Petty,* 1998]. Therefore, the second step modified the cut-off threshold for rain/no-rain classification by using a PCT criterion instead of a straight T_b cut-off. These modifications were implemented in 2004 for the version 6 TMI product and third release of AMSR-E products with a slight difference for each product. The significant changes implemented for the latest version (version 7) of the GPROF TMI ocean algorithm involves addition of the probability of precipitation parameter, wherein pixels are not screened before Bayesian scheme. The algorithm developers recommend using 50% probability of rainfall threshold within the FOV when comparing with instantaneous PR and TMI rain rates. For the TMI coastal algorithm, a change in the land/ocean classification has been implemented [*Zagrodnik and Jiang*, 2013].

1.4.5. Global Satellite Mapping of Precipitation (GSMaP) Algorithm

The GSMap algorithm was developed by the Earth Observation Research Center, Japan Aerospace Exploration Agency (JAXA/EORC), and has been further improved with the use of PR measurements. Comparative studies by *Kummerow et al.* [2001] evaluated the performance of TRMM monthly rainfall estimates from both its sensors TMI and PR, which revealed a bias between both the rainfall products of nearly 30% over ocean and 26% over land (using version 5 of data products). The TRMM version 6 algorithms display improvements within level 2 surface rain retrieval algorithms based on physical principles. Results of intercomparison studies between version 5 and version 6 algorithms are presented in *Chiu et al*. [2006]. GSMaP is drawn up to the highest levels of precision and resolution with temporal resolution of 1 h and spatial resolution of 0.1°. The RNC algorithms implemented in GSMaP for over land, over ocean, and coastal regions are discussed below.

1.4.5.1. RNC Over Land

Seto et al. [2005] developed the RNC classification algorithm (version 4.5) for GSMaP that was employed in TRMM. Their study involved statistically summarizing all the TMI T_b values under no-rainfall conditions of PR 2A25, for the land regions into a database that represented both the spatial and temporal variations of T_b. This "land surface brightness temperature database" contained the spatiotemporal variations of T_b including the effects of sand and fallen snow [*Seto et al.,* 2005]. Due to the varied spatial resolutions of TMI channels among themselves as well as with PR, footprint size was defined by means of effective field of view (EFOV). PR footprints, the center of which lie within a

TMI footprint, were chosen as reference. In their study, all the PR observations within a TMI footprint that had a "no-rain" or "rain-possible" flag were adjudged to be in no-rain conditions. Their study summarized TMI observations under no-rain conditions in a database with resolution of 1 month and 1° latitude × 1° longitude. The distribution of T_b values under no-rain conditions was represented using a Gaussian distribution. The mean (μ) and standard deviation (σ) of 85 GHz (V) T_b were calculated to represent the distribution and stored in the database.

Seto et al. [2005] proposed two RNC methods (named as M1 and M2) for real-time use. The first method (M1) used the parameters estimated from the database of TMI T_b under no-rain conditions. The value for $T_{b, \text{Estimated}}$ was fixed as equivalent to μ and the threshold of scattering was judged at $k_0\sigma$ where k_0 was a constant in space and time. The thresholds for M1 differed with month and grid. This was an improvement over the threshold of *Adler et al.* [1994], which remained fixed at a constant value of 251 K. M2 considered a linear regression fit using least mean square error, between T_b (21.3 V) and T_b (85.5 V), both under no-rain conditions, using the database.

$$\left(T_{b,85.5\text{V}}\right)_{\text{NoRain}} \sim a + b\left(T_{b,21.3\text{V}}\right)_{\text{NoRain}} \quad (1.14)$$

The subscript denotes observations conducted under no-rain / clear sky conditions. If σ_e is the standard deviation of

residuals of equation and k_0 is a constant in both space and time, the pixel fulfilling the criterion of equation (1.11) is adjudged as containing a rainfall signature:

$$\left(T_{b,85.5\text{V}}\right)_{\text{Estimated}} - \left(T_{b,85.5\text{V}}\right)_{\text{Observed}} > k_0\sigma_e \quad (1.15)$$

The number of rain pixels increased or decreased depending on the value of k_0, which varied with regions and seasons. The usual practice was to affix a constant value for k_0 for simplicity reasons. For GSMaP, the value of k_0 adopted was 3.5 and no desert/snow masks were employed as in *Grody* [1991]. The proposed RNC for version 4.7 was the same as that of version 4.5 with the only difference being in the retrieval part. These RNC methods are also known as PR-dependent methods as they cannot be applied to other microwave radiometers not accompanied by spaceborne precipitation radar. The methods (M1 and M2) were modified with an aim to make the RNC methods independent of PR so that these could be applied to data from other microwave radiometers as well. Comprehensive details regarding these can be found in *Seto et al.* [2009].

1.4.5.2. RNC Over Oceans

Over oceans, GSMaP adopted the method of *Kida et al.* [2009]. Their study employed two stages for detection of rain and no-rain footprints, as shown in Figure 1.7. In the first stage, deep rain pixels were
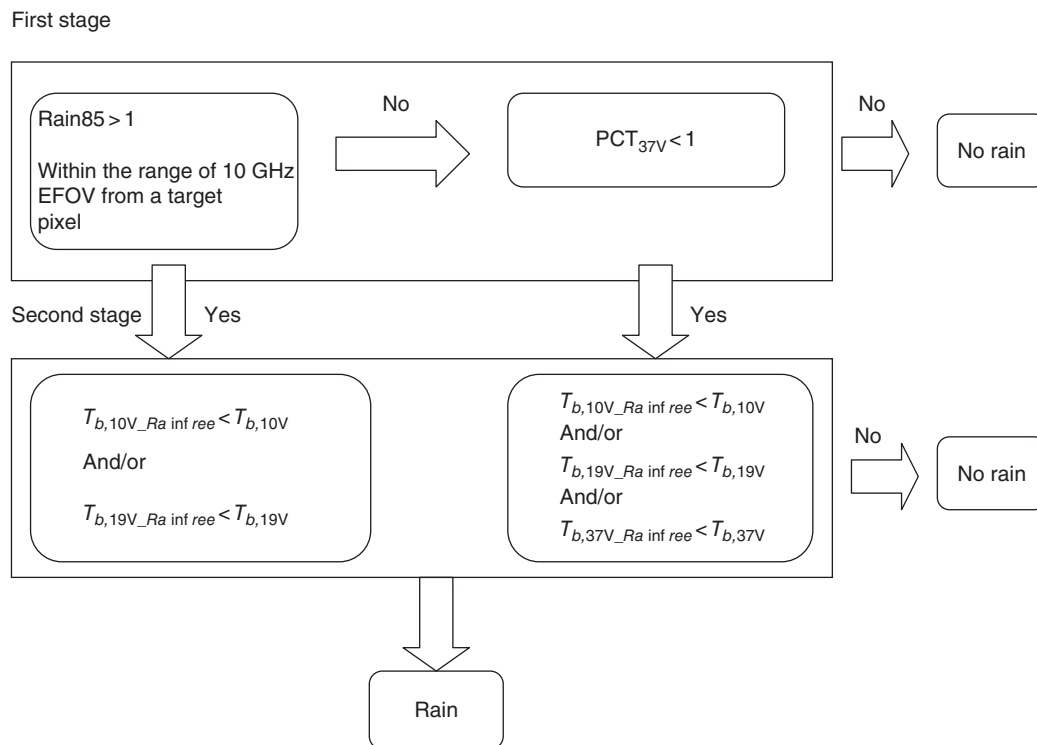

Figure 1.7 Flowchart for RNC classification used in GSMaP [*Kida et al.*, 2009].

determined by T_b from 85 GHz (V) scattering signature, and shallow rain pixels were determined with normalized polarization difference at 37 GHz (V). The study considered all the pixels of 85 GHz (V) lying within the EFOV of 10 GHz (V) pixel. The condition for detection of deep rain pixel was then fixed as the existence of one or more pixels of 85 GHz (V) within the EFOV of 10 GHz (V), having a rain rate > 1mm/h (rain 85 pixels). The study classified the target pixel (central pixel) as deep rain pixel upon fulfilling the above condition. If not, the normalized PCT [*Petty*, 1994] as given by equation 1.12 was used to check the existence of shallow rain:

$$PCT_{37V} = \frac{T_{b,37V} - T_{b,37H}}{T_{b,37V\_Rain free} - T_{b,37H\_Rain free}}. \quad (1.16)$$

Based on the results of the first stage, their study checked emission signatures from raindrops in the second stage. The three checks used in the second stage are shown in Figure 1.7 from which it can be seen that T_b values of channels 19 GHz (V), 10 GHz (V), and 37 GHz (V) were used.

Kida et al. [2009] proposed modifications for the RNC method of GSMaP in order to use T_b from 37 GHz (V) more efficiently. Their study was essentially a PR-dependent method wherein the level 2 standard product 2A25 [*Iguchi,* 2007] was used as the validation product. Their study modified two conditions used in the first stage of GSMaP. In the original GSMaP algorithm,

for the first stage, in the presence of pixels whose rain 85 > 1 mm/h within the EFOV of 10 GHz (V), the central target pixel was identified as a deep rain pixel, even if it may actually be a shallow rain pixel. This led to misclassification of most of the shallow rain pixels as no-rain pixels (Figure 1.8). *Kida et al.* [2009] modified the first-stage algorithm by checking the rain rate of 85 GHz (V) T_b pixel just for the target pixel, to avoid misclassification of shallow rain pixels as deep rain pixels. The second modification was use of 37 GHz (V) T_b instead of normalized PCT to detect shallow rain. This was because T_b at 37 GHz (H) was known to be more sensitive to wind speed than T_b at 37 GHz (V). With increase in wind speed, T_b at 37 GHz (H) increases more than T_b at 37 GHz (V). And in the case of an extraordinary event such as a typhoon, characterized by strong wind speed, PCT (using 37 GHz) will be less than 1, leading to misclassification of shallow rain in windy regions. Hence, their study preferred Tb from 37 GHz (V) channel, which was less sensitive to wind speed variations.

1.4.5.3. RNC Over Coasts

Over coastal areas, GSMaP used the RNC algorithm proposed by *Kubota et al.* [2007]. Their study was an improvement over the RNC detection method of *McCollum and Ferraro* [2005], which detected precipitating areas using PCT index at 85 GHz (V) and a decision tree of several empirical conditions for TMI T_b's. *Kubota et al.* [2007] used the condition of surface temperature < 273.2 K for flagging no-rain pixels over coastal areas.
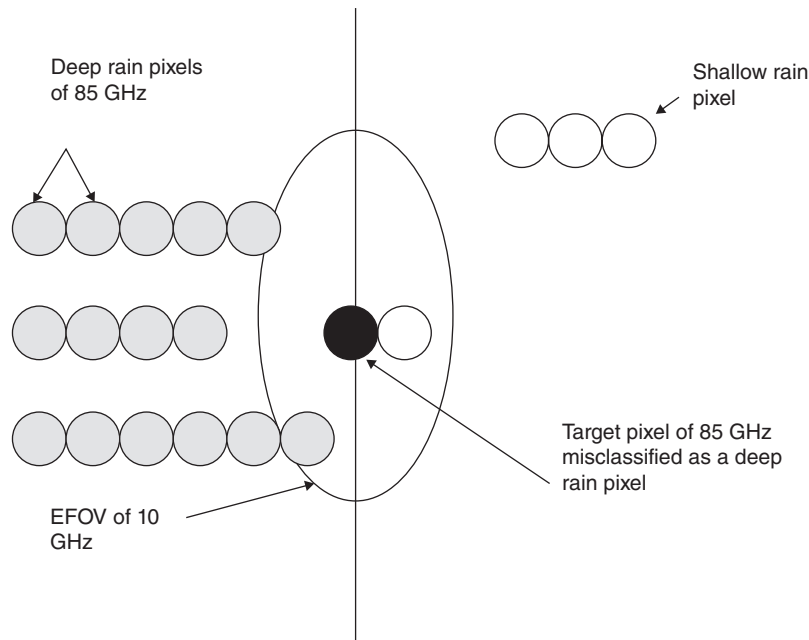
Figure 1.8 Example of a shallow rain pixel being misclassified as a deep rain pixel [*Kida et al.*, 2009].

The previously employed condition of $T_{b,85H} > 257$, $T_{b,22V} < 269.1$ leads to false rainfalls during the winter in midlatitude coastal areas and hence is avoided. *Kubota et al.* [2007] classified ambiguous class into "possible rain" and "no-rain" classes. Instead of using a PCT cutoff threshold, their study applied a scattering index threshold of RainPCT85 > 1, to possible rain cases. Here, rainPCT85 stands for rain rate from PCT index calculated using 85 GHz (V) channel frequency. Selection of a suitable threshold for RNC classification is as important as deriving the algorithm itself. For the GMSaP algorithm, *Kida et al.* [2008] proposed a parameterization of rain/no-rain threshold value of cloud liquid water as a function of storm height based on CloudSat precipitation product and the cloud liquid water derived from Aqua/AMSRE.

1.5. RNC PERFORMANCE ANALYSIS

RNC classification is a typical example for dichotomous classification having just two probabilities of either zero (denoting "no") or unity (denoting "yes") whose result can be expressed in 2 × 2 contingency matrix as shown in Table 1.2. In Table 1.2, the element *a* denotes the number of correct (or yes) forecasts of an observed event, *c* refers to the number of events that occurred but were not forecast, *b* is the number of forecasts of events that did not occur, and *d* is the number of correct forecasts of events that did not occur. It should be noted that Table 1.2 depicts dichotomous classification wherein collocated TMI and PR observations are analyzed assuming PR observations to be "true" or near perfect. Some studies increase the resolution of low-frequency channels by linear interpolation to match the resolution of 85 GHz (V) channels. Data collocation can then be performed using the geolocation information from TRMM PR and TMI data set to assign a TMI pixel at the 85 GHz (V) resolution as the nearest neighbor for every PR pixel in an orbit [*Gopalan et al.,* 2010; *Indu and Kumar,* 2013]. Data collocation has also been carried out by aggregating all of the PR observations within a TMI footprint before skill score calculations [*Seto et al.,* 2005]. This section

Table 1.2 Layout of contingency matrix[a]

	Event Observed	
	Rain Judged by PR (Yes)	No Rain Judged by PR (No)
Event Forecast		
Rain judged by TMI (Yes)	a	b
No rain judged by TMI (No)	c	d

[a]Assuming that the rainflag by PR is near perfect and can be used as validation data.

discusses some of the statistical descriptors used to analyze performance of this binary classification. The commonly used indices for RNC accuracy assessment are summarized in Table 1.3.

The most commonly used indices are the probability of detection (POD) or prefigurance [*Panofsky et al.*, 1965] and the false alarm ratio (FAR). POD is the likelihood that an event would be estimated, given that it occurred, whereas FAR is an element of the conditional distribution of events given the estimate. Due to the negative orientation of FAR, smaller values indicate better estimates [*Wilks*, 1995]. Another measure used to compare the average estimate with the average observations is the frequency bias (*B*). *B* signifies the ratio of number of yes estimates to the number of yes observations. In this measure less than one indicates underestimation and greater than one indicates overestimation. The threat score (TS) or critical success index (CSI) indicates the number of correct yes estimates divided by the total number of occasions on which the event was estimated or observed [*Wilks*, 1995]. CSI has been widely used as a performance measure for rare events (as rainfall extremes) as it does not use the content of null events, as in POD and FAR [*Montero-Martinez et al.*, 2012]. These indices help to answer questions regarding meteorological aspects such as: (1) How reliable is a product in detecting precipitation? (obtained using POD); (2) How to quantify overall bias of satellite estimates using ground truth? (obtained using *B*); (3) How often does a product indicate precipitation during nonprecipitating scenarios? (obtained using FAR).

Performance analysis of binary classification can also be characterized using relative accuracy measures or skill scores. Skill scores quantify the agreement between forecast and observations [*Tartaglione*, 2010]. A skill score is the ratio of differences [*Stanski et al.*, 1989; *Wilks*, 1995] of scalar representations of the classification performance. An estimating scheme cannot be useful if it yields skill scores that can be obtained by less sophisticated estimating procedures [*Storch and Zwiers,* 1999]. It is to be noted that no single skill score can be used to indicate forecast skill. Hence, various skill scores or relative accuracy measures are derived from the contingency table. Different skill scores perform differently. Some of the skill scores used are Heidke skill score (HSS), Kuiper skill score (KSS), Gilbert skill score (GSS), and odd's ratio skill score (ORSS). The reference accuracy measure in the HSS [*Heidke,* 1926] is the hit rate of random estimates, subject to the constraint that the marginal distributions of estimates and observations characterizing the contingency table for the random estimates are the same as the marginal distributions in the actual verification data set [*Wilks*, 1995]. HSS is a generalized skill score that tends to eliminate classifications occurring purely due to chance. Thus, perfect classification yields HSS value of 1, which implies

Table 1.3 List of performance statistics used in the study

Serial No.	Performance Measure	Formula	Range
1.	Probability of detection (POD)	$\dfrac{a}{a+c}$	[0, 1]
2.	Threat score (TS) of Critical success index (CSI)	$\dfrac{a}{a+b+c}$	[0, 1]
3.	Miss rate (M)	$1-H$	[0, 1]
4.	False alarm ratio (FAR)	$\dfrac{b}{a+b}$	[0, 1]
5.	Heidke skill score (HSS)	$\dfrac{2(ad-bc)}{(a+c)(c+d)+(a+b)(b+d)}$	[$-\infty$, 1]
6.	Kuiper skill score (KSS)	$\dfrac{ad-bc}{(a+c)(b+d)}$	[-1, 1]
7.	Percent correct (PC) or hit rate (H)	$\dfrac{a+d}{n}$	[0, 1]
8.	Bias (B)	$\dfrac{a+b}{a+c}$	[0, ∞]
9.	Gilbert skill score (GSS)	$\dfrac{a-a_r}{a+b+c-a_r}$ $\quad a_r=\dfrac{(a+b)(a+c)}{n}$	[0, 1]
10.	Odds ratio skill score (ORSS)	$\dfrac{ad-bc}{ad+bc}$	[-1, 1]
11.	Log odds ratio	$\ln(a)+\ln(d)-\ln(b)-\ln(c)$	[$-\infty$, ∞]

that the performance of the classification is 100%. Another popular skill score, which was proposed by Pierce [1884] is the Kuiper skill score, known by many names such as true skill statistic [*Flueck,* 1987], Pierce skill score, Kuiper's performance index [*Murphy and Daan,* 1985], and so forth. KSS does not depend on climatological event frequency. Perfect classification results in a KSS value of 1, whereas inferior classification can even take negative values. The highlight of KSS is that both random and constant estimates receive a zero score. It also tends to zero if the event under consideration is rare in nature. Both HSS and KSS can be extended to multicategory estimate as well. Gilbert skill score, known as equitable threat score (ETS), was proposed by *Gilbert* [1884]. He proposed that, when the expected number of hits obtained by a random estimating system with the same estimate rate of occurrence as the actual estimating system is subtracted from both the numerator and denominator, it results in a measure known popularly as ETS or Gilbert skill score (GSS) [*Hogan et al.*, 2010]. GSS is widely used to operationally assess the performance in forecasting events over a range of thresholds [*Tartaglione*, 2010]. A perfect estimate gives GSS a value of 1, whereas a worst estimate gives GSS a value of 0. *Doswell et al.* [1990] has proved that ETS is monotonically but nonlinearly related to the

truly equitable Heidke skill score with the relation ETS = HSS/(2-HSS). However, GSS can be a useful index only if supplemented with additional information such as the frequency of occurrence of the event [*Mason*, 1989].

The odds or risk of an event happening, denoted by ORSS, is the performance index that can be subjected to statistical significance testing. ORSS is the ratio of probability that the event will happen to the probability of it not happening. This measure depends solely on the conditional joint probabilities and not on the marginal probabilities, and is therefore independent of any bias between observations and estimates. When the hit and false alarm rates are identical, odds ratio becomes unity. ORSS varies between +1 and −1, where a score of 1 indicates perfect skill and a score of 0 represents no skill. Negative values imply that the estimate was opposite to what was originally observed. *Stephenson* [2000] stated that associated variables that give odds ratio larger than unity can be tested for significance by considering the natural logarithm of the odds ratio referred also as "log odds," which is asymptotically Gaussian distributed. Agresti [1996] stated that when any one of the cell counts is zero, the asymptotic standard error in log odds becomes infinite and the odds ratio can no longer be meaningfully tested for significance. More information regarding validation

of satellite-based precipitation estimation can be obtained from the research by the International Precipitation Working Group (IPWG) (*http://www.isac.cnr.it/~ipwg/IPWG.html*).

It should be noted that the performance of an RNC algorithm is strongly affected by the spatial and temporal scales for rainfall detection and the rainfall detection threshold. Identification of an optimum threshold for RNC classification depends on the missed rain amount, false rain amount, and most importantly on the user requirements. If the end product is to generate rain maps for flood warning, a lower threshold should be fixed for safety reasons. A larger threshold value is preferred if the resulting rain map is to be used for drought warning [*Seto et al.*, 2005]. Difference in spatial resolutions of multifrequency satellite microwave observations is a common problem in RNC classification and subsequent rainfall retrieval process. Usage of channels with larger FOV will incorporate more noise from outside the test area, thereby resulting in decreased accuracy. When the radiometer FOV is partially filled with cloud or rain, it results in beam filling effects that have been well documented in many studies [*Melitta and Katsaros*, 1995; *Greenwald et al.*, 1997; *Bremen et al.,* 2002; *Chiu et al.,* 1990; *Short and North,* 1990; *Kummerow et al.*, 1998]. Some studies have used techniques to deconvolve the TMI T_b's at 10 GHz and convolve at 21–85 GHz to a common FOV corresponding to 19 GHz (H) FOV [*Backus and Gilbert,* 1970]. A resampling technique is applied to the TMI data to perform this operation using a linear combination of nearby observations using knowledge regarding TMI antenna patterns and scan geometry. The crucial points to be considered are the parallax effects between the instruments (e.g., TMI and PR) and their antenna pattern, the inclusion of signals from outside the EFOV if footprint is defined using EFOV, beam filling effects, and the like [*Bauer et al.*, 2002]. Studies showing temporal variations of FAR and POD for various RNC algorithms were presented in *Seto et al.* [2005]. Their study revealed that diurnal variations in the physical temperature of land surface cause T_b values of no-rain pixels to be lower at night. This directly implies that at night, a constant rainfall detection threshold for T_b will tend to produce a higher FAR.

1.6. OPEN QUESTIONS

The ultimate goal of RNC classification is to produce the most accurate detection of rainfall signature from microwave footprints over any background surface (land, ocean, coast). Since the accuracy of RNC algorithms is tied to the characteristic properties of microwave data in multiple frequency channels, the need to understand and improve quality of information retrieved from various channels is obvious. There remain several open questions that need to be addressed such as uncertainty due to RNC, inability of present algorithms to detect light rain, and so forth. Here, we outline some important questions and possible future research directions.

1.6.1. Resampling/Matchup Errors

The distribution of microphysical parameters, precipitation cells, cloud cover, and associated volume absorption and scattering coefficients are subjected to large variability within a microwave radiometer footprint [*Smith and Kidder*, 1978; *Austin and Geotis*, 1978; *Mugnai and Smith,* 1988]. For quantitative assessment of rain/no-rain classification, by far the biggest issue is the nonuniform spatial resolution wherein diffraction limits the attainable resolution. Microwave footprints are characterized with large horizontal resolution (FOV). And when information from multiple frequencies having differing resolutions need to be combined to retrieve geophysical parameters, which are not necessarily homogeneous over the footprint area, the problem of resolution mismatch becomes critical. The literature presents several approaches to solve this issue in the form of simple averaging of high-resolution measurements to match the low-resolution data, matching the resolution of all the frequencies to a common 25 km spatial resolution. *Backus and Gilbert* [1970] proposed a technique for inverting seismic data in order to retrieve Earth density profiles. This technique reconstructed measurements at different resolutions from those originally sampled using a combination of oversampled measurements. Theory by *Backus and Gilbert* [1970] is being largely employed in atmospheric remote sensing applications to convolve microowave measurements to a common resolution [*Hollinger et al.*, 1987]. Another common approach being followed is averaging of inhomogeneous retrieved parameters from data of differing resolutions. However, the accuracy of retrieval is strongly influenced by input data resolution, which if not done carefully tends to incorporate errors. Further, due to the varying FOV sizes and spectral bands used by different microwave radiometers, some of the thresholds used for RNC screening are unreliable, which tends to get aggravated at the interfaces between surface types (i.e., coastline) and results in "ambiguous" classification in the resulting rainfall product. Before undertaking experiments using the plethora of available microwave products, it would be worthwhile to understand these effects.

1.6.2. Drawback of Modeling RNC Using Database

Many authors utilize a statistical database of T_b under no-rain conditions to model the nonscattering portion of 85 GHz (V) instead of using a set of sensitive channel

combinations. The creation of such a consistent database requires TRMM-like satellites without which the databases cannot be produced globally. The issue is that a database built on TRMM observations cannot be applied to areas beyond TRMM coverage area. Moreover, satellites such as GPM and MT have slightly different channel frequencies than TRMM TMI (85.5 GHz for TMI, 89.0 GHz for AMSR-E) and therefore a previously created database would need to be adjusted to suit each sensor. To overcome this problem, radiative transfer modeling of land surfaces is essential.

1.6.3. Assumption of Marshall Palmer Size Distribution for Ice

Atmospheric hydrometeors are generally nonspherical [*Pruppacher and Klett*, 1978]. The alteration of T_b measurements due to hydrometeor size, phase, layer depth, and other factors is quantified by *Mie* [1908] theory. Ice particles are complicated with unknown particle sizes, densities, and shapes, all affecting T_b. The assumption of Marshall-Palmer size distribution for ice is a result of convenience, due to the unavailability of direct measurements of ice particle sizes within convective storms. Even if the measurements existed, modeling using radiative transfer becomes highly difficult. This is why we rely on empirical relationships. For overland regions, scattering-based modeling is not very well understood. Ice particles actually found within a rainstorm have highly varying shapes and sizes that depend on atmospheric temperature and humidity. Ice particle shapes offer a crucial parameter for single scattering calculations that affects emerging radiance field [*Mugnai and Wiscombe*, 1986; *Bohren*, 1986]. Yet they remain modeled as an ensemble of spheres, despite the evidence that oriented ice particles can cause polarization difference of up to 10 K in stratiform regions associated with strong convection. When the particles causing scattering are small in size compared to the wavelength of observation, scattering is more or less assumed to be well approximated by that of a sphere of equal mass, but the actual electromagnetic solutions are completely intractable for all but a very few shapes. This area still needs to be addressed.

1.6.4. Additional Factors

Microwave sensors are relatively insensitive to low-altitude liquid-water-bearing clouds. There are no specific screens developed to reliably separate nonraining and raining clouds. Moreover, defining a suitable threshold to detect raining clouds so that it suits every climatic regime is nearly impossible due to the lack of corresponding validation data. The usual procedure for selecting a threshold is to either detect even the lightest rain at the cost of misclassifying nonraining clouds or to detect rain only above a certain threshold at the expense of eliminating light-rain pixels. The choice of either a liberal or a conservative threshold affects the accuracy of RNC and this area needs to be researched further.

Also, most of the overland precipitation retrieval algorithms rely on a fixed land-sea-coast database that might not exactly match up with what the instrument (i.e., radiometer) is viewing as it enters the decision tree classification scheme. Ambiguity is further offered to the retrieval process due to the existence of inland water bodies [*Sudradjat et al.*, 2010]. Over oceans, RNC classification is affected by strong winds that tend to impact the emitting temperature and polarization signature especially at low microwave frequencies. This in turn causes misclassification of the area as rain where no rain is present. When ocean surface is clear and calm, the emissivity will be at its lowest. In the presence of a dry atmosphere, very low T_b values can result that may again cause erroneous screening of raining area. These pose serious problems for 85 GHz scattering based techniques using single polarization temperature thresholds to delineate rain areas.

The scattering properties of each surface type are different. A database consisting of scattering properties of different land surface covers can be generated to create different SI-based RNC algorithms sensitive for each surface type. Change in land use land cover (such as deforestation) that affect scattering signatures of land covers need to be accounted. Usage of ancillary information for land surface types might improve the rain detection over problematic surfaces such as desert, semiarid regions, coastal, and inland regions. In order to develop more physically based approaches for overland precipitation retrieval, all these problematic issues need to be addressed.

1.7. CONCLUSIONS

Rainfall screening methodologies have progressed with the evolution of new microwave sensors. Over the years, RNC studies have evolved from simple relations formulated for computational expedience to more elaborate computer-intensive schemes that effectively discriminate rainfall occurrence. This chapter discussed the principles of rain/no-rain (RNC) algorithms that have been developed through the years processing data from satellite-borne passive microwave radiometers. Any screening algorithm would depend on the characteristic interaction of atmospheric constituents with the microwave frequency energy. Hence, we summarized the interaction of microwaves with major sources and sinks of microwave frequency energy such as water vapor, cloud water, cloud ice, precipitation, and the like. Two different approaches to RNC classification were presented: one

based on scattering signatures of atmospheric constituents at high microwave frequencies and the other based on emission-based techniques for over ocean rainfall delineation. We focused on the major rainfall screening techniques used for the different backgrounds of land, ocean, and coastlines. Quantifying the uncertainty caused in overland rainfall retrieval due to improper screening of raining pixels is not a trivial task owing to cluttering of microwave brightness temperature by varying overland emissivity, beam filling errors, resolution matchup errors, and the like. Often the rainfall products suffer from underestimation of warm rainfall due to low-level liquid-water-bearing clouds that go undetected by a microwave radiometer. Over the years, overland RNC algorithms have been continuously evolving to bridge the gap in bias caused between the passive and active microwave rainfall products. Such studies have made significant contributions to improve the existing RNC techniques used in prominent algorithms such as the global satellite mapping (GSMaP) and Goddard profiling algorithm (GPROF). Many recent studies have propagated the idea of RNC classification to land surfaces of small areal extent. Challenges for RNC classification include detecting shallow rainfall, improving accuracy through derivation of global threshold values, addressing the nonhomogeneity of geophysical parameters within the large field of view of microwave footprints, and using RNC screening techniques independent of PR that can be applied to satellites outside the field of view of TRMM. Future work in these directions will aim to create global RNC classification algorithms using scattering properties of different land cover types, which can be globally applied for sensors of slightly differing fields of view.

ACKNOWLEDGMENTS

REFERENCES

Adler, R. F., H.-Y. M. Yeh., N. Prasad, W.-K. Tao, and J. Simpson (1991), Microwave simulations of a tropical rainfall system with a three dimensional cloud model, *J. Appl. Meteor.*, *30*, 924–953.

Adler, R., A. Negri, P. Keehn, and I. Hakkarinen (1993), Estimation of monthly rainfall over Japan and surrounding waters from a combination of low-orbit microwave and geosynchronous IR data, *J. Appl. Meteorol.*, *32*, 335–356, doi:10.1175/1520-0450(1993)032<0335:EOMROJ>2.0.CO;2.

Adler, R., G. J. Huffman, and R. R Keehn (1994), Global tropical rain estimates from microwave-adjusted geosynchronous IR data, *Remote Sens. Rev.*, *11*, 125–152.

Agresti, A. (1996), An Introduction to Categorical Data Analysis, New York, USA, Wiley Interscience Publication.

Anagnostou, E. N., and C. Kummerow (1997), Stratiform and convective classification of rainfall using SSM/I 85-GHz brightness temperature observations., *J. Atmos. Oceanic Technol.*, *14*, 570–575.

Austin, P. M., and S. G. Geotis (1978), Evaluation of the quality of precipitation data from a satellite borne radiometer. Final Report, NASA Contract NSG-5024., MIT, Cambridge, MA.

Backus, G., and F. Gilbert (1970), Uniqueness in the inversion of inaccurate gross earth data, *Philos. Trans. Roy. Soc. London*, *A266*, 123–192.

Barrett, E. C., and D. W. Martin, (1981), *The Use of Satellite Data in Rainfall Monitoring*, Academic, San Diego.

Barrett, E. C., C. Kidd, and Bailey J. O., (1988), The special sensor microwave imager: a new intstrument with rainfall monitoring potential, *Int. J. Remote Sensing*, *9*, 1943–1950.

Bauer, P (2001), Including a melting layer in microwave radiative transfer simulation for clouds., *Atmos. Res.*, *57*, 9–30.

Bauer, P., J. F. Mahfouf., W. S. Olson., F. S. Marzano, F. S., S. Di Michele., A. Tassa., and A. Mugnai (2002), Error analysis of TMI rainfall estimates over ocean for variational data assimilation, *Q. J. R. Meteorol. Soc.*, *120*, 1367–1388.

Bauer, P., and P. Schluessel (1993), Rainfall, total water, ice water and water vapor over the sea from polarized microwave simulations and SSM/I data., *J. Geophys. Res.*, *98*(D11), 737–759.

Bennartz, R. (1999), On the use of SSM/I measurements in coastal regions, *J. Atmos. Oceanic Technol.*, *18*, 1838–1855.

Biscaro, T. S., and C. A. Morales (2007), Continental passive microwave based rainfall estimation algorithm: Application to the Amazon basin., *J. Appl. Meteor. Climatol.*, *47*, 1962–1981.

Bohren, C. F (1986), Absorption and scattering of light by non-spherical particles. Extended abstracts, Sixth Conf. on Atmos. Rad., Williamsburg, VA, Amer. Meteor. Soc., pp. 1–7.

Bremen, L. V., E. Ruprecht, and A. Macke (2002), Errors in liquid water path retrieval arising from cloud inhomogeneities: The beam-filling effect. *Meteor. Z.*, *11*, 13–19.

Burke, W. J., T. Schmugge, and J. F. Paris (1979), Comparison of 2.8 and 28 cm microwave radiometer observations over soils with emission model calculation., *J. Geophys. Res.*, doi:10.1029/0JGREA0000840000C1000287000001.issn:0148-0227.

Chandrasekhar, S. (1960), *Radiative Transfer*, Oxford University Press, Oxford.

Chelton, D. B., and M. H. Freilich (2005), Scatterometer-based assessment of 10m wind analyses from the ECMWF and NCEP numerical weather prediction models, *Mon. Wea. Rev.*, *133*, 409–429.

Chiu, L. S., G. R. North, D. A. Short, and A. McConnell (1990), Rain estimation from satellites: Effect of finite field of view, *J. Geophys. Res.*, *95*, 2177–2185.

Chiu, L. S., D.-B. Shin, and J. Kwaitkowski (2006), *Surface rain rates from Tropical Rainfall Measuring Mission satellite algorithms, Earth Science Satellite Remote Sensing*, Vol. I, edited by J. Qu, et al., Springer-Tsinghua University Press, Berlin, pp. 317–336.

Conner, M. D., and G. W. Petty (1998), Validation and intercomparison of SSM/I rain-rate retrieval methods over the continental United States, *J. Appl. Meteor.*, *37*, 679–700.

Coppens, D., Z. S. Haddad, and E. Im (2000), Estimating the uncertainty in passive microwave rain retrieval. *J. Atm. Oceanic. Technol.*, *17*, 1618–1629.

Derr, V. E. (1972), *Remote Sensing of the Troposphere*, U.S. Govt. Printing Office, Washington, D.C.

Dinku, T., and E. N. Anagnostou (2005), Regional differences in overland rainfall estimation from PR-calibrated TMI algorithm, *J. Appl. Meteor.*, *44*, 189–205.

Doswell, C. A. III., R. Davies-Jones., and D. L. Keller (1990), On summary measures of skill in rare event forecasting based on contingency tables, *Weath. Forecasting.*, *5*, 576–586.

Elachi. C. (1987), *Introduction to the Physics and Techniques of Remote Sensing*, pp. 32–37, Wiley, New York.

England, A. W. (1976), Relative influence upon microwave emissivity of fine-scale stratigraphy, internal scattering and dielectric properties, *Pure Appl. Geophys.*, *114*, 287–299.

English, S. J. (1999), Estimation of temperature and humidity profile information from microwave radiances over different surface types, *J. Appl. Meteor.*, *38*(10), 1526–1541.

Evans. K. F., J. Turk, T. Wong, and G. L. Stephens (1995), A Bayesian approach to microwave precipitation profile retrieval, *J. Appl. Meteor.*, *34*, 260–279.

Ferraro, R. R. (1997), Special sensor microwave imager derived global rainfall estimates for climatological applications, *J. Geophys. Res.*, *102*, 16715–16735.

Ferraro, R. R., and G. F. Marks (1995), The development of SSM/I rain rate retrieval algorithms using ground based radar measurements, *J. Atmos. Oceanic Technol.*, *12*, 755–770, doi:10.1175/1520-0426(1995)012<0755:TDOSRR>2.0.CO;2.

Ferraro, R. R., N. C. Grody, and J. A. Kogut (1986), Classification of geophysical parameters using passive microwave satellite measurements, *IEEE Trans. Geosci. Remote Sens.*, *24*, 1008–1013.

Ferraro, R. R., N. C. Grody, and G. G. Marks (1994), Effects of surface conditions on rain identification using the DMSP-SSM/I, *Remote Sens. Rev.*, *11*, 195–209.

Ferraro, R. R., F. Weng, N. C. Grody, and A. Basist (1996), An eight-year (1987–1994) time series of rainfall, clouds, water vapor, snow cover, and sea-ice derived from SSM/I measurements, *BAMS*, *77*, 891–905.

Ferraro, R. R., E. A. Smith, W. Berg, and G. J. Huffman (1998), A screening methodology for passive microwave precipitation retrieval algorithms, *J. Atmos. Sci.*, *55*, 1583–1600. doi:10.1175/1520-

Ferraro, R. R., E. A. Smith, W. Berg, and G. Huffman (2005), NOAA operational hydrological products derived from the AMSU, *IEEE Trans. Geosci. Remote Sens.*, *43*, 1036–1049.

Ferrazoli, P., J. P. Wigneron, L. Guerriero, and A. Chanzy (2000), Multifrequency emission of wheat modeling and application, *IEEE Trans. Geosci. Remote Sens.*, *38*, 2598–2607.

Fraser, R. S. (1975), Interaction mechanisms—within the atmosphere, in *Manual of Remote Sensing*, Vol. 1, pp. 181–233, edited by F. J. Janza, *Theory, Instruments and Techniques*, American Society of Photogrammetry, Falls Church, Va.

Fulton, R., and G. M. Heymsfield (1991), Microphysical and radiative characteristics of convective clouds during COHMEX, *J. Appl. Meteor.*, *30*, 98–116.

Fung, A. K. (1994), *Microwave Scattering and Emission Models and Their Applications*, Artech House, pp. 277–303, Boston.

Gilbert, G. F. (1884). Finley's tornado predictions. *Amer. Meteor. J.*, *1*, 166–172.

Gopalan, K., N.-Y. Wang, R. Ferraro, and C. Liu (2010), Status of the TRMM 2A12 land precipitation algorithm, *J. Atmos. Oceanic Technol.*, *27*, 1343–1354.

Gorelik, A. G., V. V. Kalashnikov, B. G. Kutuza, and V. I. Semiletov (1971), Measurements of space distribution of brightness temperatures of clouds and rain at 0.8 and 1.35 centimeter wavelengths, *Advances in Satellite Meteorology*, Wiley, New York.

Grecu, M., and E. N. Anagnostou (2001), Overland precipitation estimation from the TRMM passive microwave observations, *J. Appl. Meteor.*, *40*, 1367–1380.

Greenwald, T. J., S. A. Christopher, and J. Chou, (1997), Cloud liquid water path comparisons from passive microwave and solar reflectance satellite measurements: Assessment of sub-field-of-view cloud effects in microwave retrievals, *J. Geophys. Res.*, *102*, 19,585–19,596.

Grody, N. C. (1991), Classification of snow cover and precipitation using the Special Sensor Microwave Imager, *J. Geophys. Res.*, *96*, 7423–7435.

Guillou, C., S. J. English, C. Prigent, and D. C. Jones (1996), Passive microwave airborne measurements of the sea surface response at 89 and 157 GHz, *J. Geophys. Res.*, *101*(C5), 3775–3788.

Gunn, K. L. S., and T. W. R. East (1954), The microwave properties of precipitation particles, *Q. J. Roy. Meteorol. Soc.*, *80*, 522–545.

Hansen, J. E., and L. D. Travis (1974), Light scattering in planetary atmospheres, *Spa. Sci. Rev.*, *16*, 527–610.

Heidke, P. (1926), Berechnung des Erfolges und der Gute der Windstarkevorhersagen in Sturnwarnungsdienst, *Geografiska Annaler*, *8*, 301–349.

Hogan, R. J., C. A. T. Ferro, I. T. Jolliffe, and D. B. Stephenson (2010), Equitability revisited: Why the "equitable threat score" is not equitable, *Weather Estimating*, *25*(2), 710–726, doi:10.1175/2009WAF2222350.1.

Hollinger, J., R. Lo., G. Peo., R. Savage., and J. Pierce (1987), *The Special Sensor Microwave/Imager's User's Guide*, *Naval Research Laboratory Technical report*, pp. 1–120, Nav. Res. Lab., Washington, D. C.

Huang, R., and K. N. Liou (1983), Polarized microwave radiation transfer in precipitating cloudy atmospheres: Applications to window frequencies, *J. Geophys. Res.*, *88*, 3885–3893.

Huffman, G. J., and R. F. Adler (1993), Precipitation estimation from SSM/I data with the Goddard Scattering Algorithm. Proc. Shared Proceeding Network SSM/I Algorithm Symp., Monterey, CA, Fleet Numerical Oceanography Center [available from Dudley Knox Library, Naval Postgraduate School, 411 Dyer Rd., Monterey, CA 93943].

Iguchi, T. (2007), Space-borne radar algorithms, in *Measuring Precipitation from Space-EURAINSAT and the Future*, edited by V. Levizzani, P. Bauer, and F. J. Turk, pp. 199–212, Springer, New York.

Indu, J. and D. N. Kumar (2013), Copula based modeling of TRMM TMI brightness temperature with rainfall type, *IEEE Trans. Geosci. Remote Sens*, doi:10.1109/TGRS.2013.2285225.

Janssen, M. A. (1993), *Atmospheric Remote Sensing by Microwave Radiometry*, Wiley, New York.

Karstens, U., C. Simmer, and E. Ruprecht (1994), Remote sensing of cloud liquid water, *Meteor. Atmos. Phys.*, *54*, 157–171.

Kida, S., S. Shige, T. Manabe, T. S. L'Ecuyer, and G, Liu (2008), Validation of rain/no-rain threshold value of cloud liquid water for microwave precipitation retrieval algorithm using CloudSat precipitation product, *Proc. SPIE7152, Remote Sensing of Atmosphere and Clouds II*, 715209, doi:10.1117/12.804924.

Kida, S., S. Shige, T. Kubota, A. Aonashi, and K. Okamoto (2009), Improvements on rain/no-rain classification methods for microwave radiometer observations over the ocean using a 37 GHz emission signature, *J. Meteor. Soc. Jpn.*, *87A*, 165–181.

Kidd, C. and E. C. Barrett (1990), The use of passive microwave imagery in rainfall monitoring, *Remote Sens. Rev.*, *4*, 415–450.

Kidder, S. Q., and T. H. Vonder Haar (1995), *Satellite Meteorology-An Introduction, Academic*, San Diego.

Kidder, S. Q., and T. H. Vonder Haar (1977), Seasonal oceanic precipitation frequencies from Nimbus 5 microwave data, *J. Geophys. Res.*, *82*, 2083–3086.

Klein, L. A., and C. T. Swift (1977), An improved model for the dielectric constant of sea water at microwave frequencies, *IEEE J. Oceanic Eng.*, *2*, 104–111.

Kubota, T., et al. (2007), Global precipitation map using satellite-borne microwave radiometers by the GSMaP project: production and validation, *IEEE Trans. Geosci. Remote Sens.*, *45*, 2259–2275.

Kummerow, C. (2001), The evolution of the Goddard Profiling Algorithm (GPROF) for rainfall estimation from passive microwave sensors, *J. Appl. Meteorol.*, *40*, 1801–1820, doi:10.1175/1520-0450(2001)040<1801:TEOTGP>2.0.CO;2.

Kummerow, C., and J. A. Weinman (1988), Determining microwave brightness temperatures from precipitating horizontally finite and vertically structured clouds, *J. Geophys. Res.*, *93*, doi: 10.1029/88JD01623.

Kummerow, C., and L. Giglio (1994), A passive microwave technique for estimating rainfall and vertical structure information from space. Part I: Algorithm description, *J. Appl. Meteor.*, *33*, 3–18.

Kummerow, C., W. S. Olson., and L. Giglio (1996), A simplified scheme for obtaining precipitation and vertical hydrometeor profiles from passive microwave sensors, *IEEE Trans. Geosci. Remote Sens.*, *34*, 1213–1232, doi:10.1109/36.536538.

Kummerow C., W. Barnes T. Kozu J. Shiue, and J. Simpson (1998), The Tropical Rainfall Measuring Mission (TRMM) sensor package, *J. Atmos. Oceanic Technol.*, *15*, 809–817, doi:10.1175/1520-0426(1998)015<0809:TTRMMT>2.0.CO;2.

Kummerow, C., W. S. Olson., and L. Giglio (2001), The evolution of the Goddard Profiling Algorithm (GPROF) for rainfall estimation from passive microwave sensors, *J. Appl. Meteor.*, *40*, 1801–1820.

Kummerow, C., W. Berg, J. T. Stahle, and H. Masunaga (2006), Quantifying global uncertainties in a simple microwave rainfall algorithm, *J. Atmos. Oceanic. Technol.*, *23*, 23–37.

Lee, T. H., J. E. Janowiak., and P. A. Arkin (1991), *Atlas of Products from the Algorithm Intercomparison Project 1: Japan and Surrounding Oceanic Regions*, June - August 1989, University Corporation for Atmospheric Research, Washington, DC.

Levizzani, V., and A. Gruber (2007), The International Precipitation Working Group: A bridge towards operational applications, in *Measuring Precipitation from Space: EURAINSAT and the Future*, edited by Levizzani, Turk and Bauer, pp. 705–712, Springer, New York.

Lin, X., and A. Y. Hou (2008), Evaluation of coincident passive microwave rainfall estimates using TRMM PR and ground measurements as references, *J. Appl. Meteor. Climatol.*, *47*, 3170–3187.

Liou, K.-N (1980), *An Introduction to Atmospheric Radiation*, Academic, New York.

Lovejoy, S., and G. L. Austin (1980), The estimation of rain from satellite-borne microwave radiometers, *Quart. J. Roy. Meteor. Soc.*, *106*, 255–276.

Marzano F. S., A. Mugnai, E. A. Smith, X. Xiang, J. Turk, and J. Vivekanandanan (1994), Active and passive remote sensing of precipitating storms during CaPE. Pan II: Intercomparison of precipitation retrievals from AMPR radiometer and CP-2 radar, *Meteorol. Atmos. Phys.*, *10*, 29–54.

Mason I. B (1989), Dependence of the critical success index on sample climate and threshold probability, *Aust. Meteor. Mag.*, *37*, 75–81.

McCollum, J., and R. R. Ferraro (2003), The next generation of NOAA/NESDIS SSM/I, TMI and AMSR-E microwave land rainfall algorithms, *J. Geophys. Res.*, *108*, 8382–8404.

McCollum, J., and R. R. Ferraro (2005), Microwave rainfall estimation over coasts, *J. Atmos. Ocean. Technol*, *22*, 497–512.

Melitta, J., and K. B. Katsaros (1995), Using coincident multispectral satellite data to assess the accuracy of special sensor microwave imager liquid water path estimates, *J. Geophys. Res.*, *100*, 16,333–16,339.

Mie, G. (1908), Beitrage zur optic truber median, speziell kolloidaler metallosunger (Contribution on the optics of scattering media, special colloidal metal solutions), *Ann. Phys.*, *25*, 377–445.

Montero-Martinez, G., V. Zarraluqui-Such, and F. Garcia-Garcia (2012), Evaluation of 2B31 TRMM product rain estimates for single precipitation events over a region with complex topographic features, *J. Geophys. Res.*, *117*, D02101, doi:10.1029/2011JD16280.

Mugnai A., and E. A. Smith (1988), Radiative transfer to space through a precipitation cloud at multiple microwave frequencies. Part I: Model description, *Am. Meteor. Soc.*, 1055–1073.

Mugnai A., and W. J. Wiscombe (1986), Scattering from non-spherical Chebyshev particles. Part I: Cross sections, single-scattering albedo, asymmetry factor, and backscattered fraction, *Appl. Opt.*, *25*, 1235–1244.

Mugnai A., E. A. Smith, and G. J. Tripoli (1993), Foundations for statistical-physical precipitation retrieval from passive microwave satellite measurements. Part II: Emission source and generalized weighing function properties of a time-dependent cloud-radiation model, *J. Appl. Meteor.*, *32*, 17–39.

Murphy, A. H., and H. Daan (1985), Forecast evaluation. *Probability Statistics, and Decision Making in the Atmospheric Sciences*, edited by A. H. Murphy and R. W. Katz, Boulder, CO, pp. 379–437, Westview Press.

Njoku, E. G. (1982), Passive microwave remote sensing of the earth from space—A review, *Proc. IEEE*, *70*, 728–750.

Njoku, E.G., and J. A. Kong (1977), Theory for passive microwave remote sensing of near-surface soil moisture, *J. Geophys. Res.*, *82*, 3108–118.

Olson, W. S. (1987), Estimation of rainfall rates in tropical cyclones by passive microwave radiometry, Ph.D. thesis, Univ. of Wisc., Madison.

Panofsky, H. A., and G. W. Brier (1965), Some applications of statistics to meteorology, The Pennsylvania State University, University Park, PA, 224.

Paris, J. F. (1971), Transfer of thermal microwaves in the atmosphere, Dept. of Meteorology, Texas A and M Univ., College Station, Tex.

Panofsky, H. A., and G. W. Brier (1965), Some applications of statistics to meteorology, The Pennsylvania State University, University Park, PA, 224.

Pierce C. S. (1884), The numerical measure of the success of predictions, *Science*, *4*, 453–454.

Pellerin, T., J.-P. Wigneror, J.-C. Calvet, and P. Waldteufel (2003), Global soil moisture retrieval from a synthetic L-band brightness temperature data set, *J. Geophys. Res.*, *108*, 4364, doi:10.1029/2002JD003086.

Petty, G. (1994), Physical retrievals of over-ocean rain rate from multichannel imagery. Part I: Theoretical characteristics of normalized polarization and scattering indices, *Meteor. Atmos. Phys.*, *54*, 79–99.

Prigent, C., W. B. Rossow, and E. Matthews (1998), Global maps of microwave land surface emissivities: Potential for land surface characterization, *Radio Sci.*, *33*, 745–751.

Pruppacher, H. R., and J. D. Klet (1978), *Microphysics of Clouds and Precipitation*, *Reidel*, Dordrecht.

Savage, R. C. (1976), The transfer of thermal microwaves through hydrometeors, Ph.D. thesis, Dept. of Meteorology, University of Wisc., Madison.

Savage, R. C. (1978), The radiative properties of hydrometeors at microwave frequencies, *J. Appl. Meteorol*, *17*, 904–911.

Savage, R. C., E. A. Smith, and A. Mugnai (1995), Concepts for a geostationary imaging sounder (GeoMIS), in *Preprints of the International Geoscience and Remote Sensing Symposium* (10–14 July, Firenze, Italy), Vol. *1*, pp. 652–654.

Schwiesow, R. L (1972), Atomic, molecular, particulate, and collective generalized scattering, in *Remote Sensing of the Troposphere. Environmental Research Laboratories*, NOAA, Boulder, Col., Chapter 10.

Seto, S., N. Takahashi, and T. Iguchi (2005), Rain/no-rain classification methods for microwave radiometer observations over-land using statistical information for brightness temperatures under no-rain conditions, *J. Appl. Meteor.*, *44*, 1243–1259.

Seto, S., T. Kubota, T. Iguchi, N. Takahashi, and T. Oki (2009), An evaluation of over-land rain rate estimates by the GSMaP and GPROF algorithms: The role of lower-frequency channels, *J. Meteorol. Soc. Jpn.*, *87A*, 183–202, doi:10.2151/jmsj.87A.183.

Shi, J., K. S. Chen, Q. Lin, T. J. Jackson, P. E. O'Neill, and L. Tsang (2002), A parameterized surface reflectivity model and estimation of bare-surface soil moisture with L-band radiometers, *IEEE Trans. Geosci. Remote Sens.*, *40*, 2674–2686.

Shifrin, K. S., and M. M. Chernyak (1968), Microwave absorption and scattering by precipitation, in *Transfer of Microwave Radiation in the Atmosphere*, pp. 69–78. Jerusalem, Israel Program for Scientific Translations.

Short, D. A., and G. R. North (1990), The beam filling error in Nimbus-5 ESMR observations of GATE rainfall, *J. Geophys. Res.*, *95*, 2187–2193.

Smith, E. A., and S. Q. Kidder (1978), A multispectral satellite approach to rainfall estimates. Presented at the 18th AMS Conf. on Radar Meteorology (28–31 March, Atlanta, GA) *The Use of Satellite Data in Rainfall Monitoring*, edited by E.C. Barrett and D. W. Martin, pp. 160–163, Acadamic, New York.

Smith, E. A., et al. (1998), Results of WetNet PIP-2 projects, *J. Atmos. Sci.*, *55*, 1483–1536.

Snider, J. B., and E. R. Westwater (1972), *Radiometry, in Remote Sensing of the Atmosphere, Environmental Research Laboratories*, NOAA, Boulder, Col., Chapter 15.

Spencer, R. W. (1986), A satellite passive 37 GHz scattering based method for measuring oceanic rain rates, *J. Climate Appl. Meteor.*, *25*, 754–766.

Spencer, R. W., W. S. Olson., Wu Rongzhang., D. W. Martin., J. A. Weinman., and D. A. Santek, (1983), Heavy thunderstorms observed over land by the Nimbus-7 scanning multichannel microwave radiometer, *J. Climat. Appl. Meteorol.*, *22*, 1041–1046, 1983.

Spencer, R. W., H. M. Goodman, and R. E. Hood (1989), Precipitation retrieval over land and ocean with the SSM/I, Part I: Identification and characteristics of the scattering signal, *J. Atmos. Oceanic Technol.*, *6*, 254–273.

Staelin, D. H. (1969), Passive remote sensing at microwave wavelengths, *Proc. IEEE*, *57*, 427–439.

Stanski, H. R., L. J. Wilson, and W. R. Burrows (1989), *Survey of Common Verification Methods in Meteorology*, WMO/TD-No.359, World Meteorological Organization, Geneva, Switzerland.

Stepanenko, V. D. (1968), Contrasts of radio brightness temperatures in clouds and precipitation, *Transfer of Microwave Radiation in the Atmosphere*, US Dept. of Commerce, Springfield, Va.

Stephenson, D. B (2000), Use of the "Ødds ratio" for diagnosing estimate skill, *Wea. Estimating*, *15*, 221–232.

Storch, H. V., and F. W. Zwiers, (1999), *Statistical Analysis in Climate Research*, Cambridge University Press, Cambridge.

Sudradjat, A., N. A. Wang, K. Gopalan, and R. R. Ferraro (2010), Prototyping a generic, unified land surface classification and screening methodology for GPM-Era microwave land precipitation retrieval algorithms, *J. Appl. Meteor. Climatol.*, *50*, 1200–1211.

Szejwach, G., R. F. Adler, I. Jobard, and R. Mack (1986), A cloud model radiative model combination for determining microwave Tb-Rain rate relations, presented at the Second Conference on Satellite Meteorology/Remote Sensing and Applications, *Am. Meteorol. Soc.*, Williamsburg, Va., May 13–16.

Tartaglione, N. (2010), Relationship between precipitation estimate errors and skill scores of dichotomous estimates, *Weather Estimate.*, *25*, 355–365.

Turk, J., E. Ebert, H.-J. Oh, B.-J. Sohn, B. Levizzani, E. Smith, and R. Ferraro (2002), Verification of an operational global precipitation analysis at short time scales, 1st Intl. Precipitation Working Group (IPWG) Workshop, Madrid, Spain, 23–27 Spet.

Ulaby, F. T., and W. H. Stiles (1981), Microwave response of snow, *Adv. Space Res.*, *1*, 131–149.

Volchok, B. A., and M. M. Chernyak (1968), Transfer of microwave radiation in clouds and precipitation, Transfer of Microwave Radiation in the Atmosphere, NASA TT F-590, pp. 90–97.

Wang, J., and D. B. Wolff (2010), Evaluation of TRMM ground-validation radar-rain errors using rain gauge measurements, *J. Appl. Meteor. Climatol.*, *49*, 310–324.

Wang, N. Y., C. Liu., R. Ferraro, E. Zipser, and C. Kummerow (2009), TRMM 2A12 land precipitation product status and future plans, *J. Meteor. Soc. Jpn*, *87A*, 237–253.

Waters, J. W. (1976), Absorption and emission by atmospheric gases, in *Methods of Experimental Physics*, Vol. 12: *Astrophysics, Part B*, edited by M. L. Meeks, Academic, New York.

Weinman, J. A., and P. J. Guetter (1977), Determination of rainfall distribution from microwave radiation measured by the Nimbus-6 ESMR., *J. Appl. Meteor.*, *16*, 437–442.

Weng, F., B. Yan, and N. C. Grody (2001), A microwave land emissivity model, *J. Geophy. Res.*, *106*, 20, 115–20 123.

Wentz, F. J (1983), A model function for ocean microwave brightness temperatures, *J. Geophys. Res.*, *88*(C3), 1892–1908.

Wentz, F. J. (1997) A well calibrated ocean algorithm for special sensor microwave/Imager, *J. Geophys. Res.*, *102*(C4), 8703–8718.

Wentz, F. J., and D. J. Cavalieri (1995), *A 20-year Geophysical Data Set from Window-Frequency Microwave Radiometers*, Remote Sensing Systems, Santa Rosa, calif.

Wilheit, T. T (1978), A review of applications of microwave radiometry to oceanography, *Boundary Layer Meteorol.*, *13*, 277–293.

Wilheit T.T (1986), Some comments on passive microwave measurement of rain, *BAMS*, *67*, 1226–1232.

Wilheit, T. T., A. T. C., Chang, M. S. V., Rao, E. B. Rodgers, and J. S. Theon, (1977), A satellite technique for quantitatively mapping rainfall rates over the oceans, *J. Appl. Meteorol.*, *16*, 551–560.

Wilheit, T. T., A. T. C. Chang, M. S. V. Rao, E. B. Rodgers, and J. S. Theon (1982), Microwave radiometric observations near 19.35, 92 and 183 GHz of precipitation in Tropical Storm cora., *J. Appl. Meteor.*, *21*, 1137–1145.

Wilheit, T. T., A. T. C. Chang, and L. S. Chiu (1991), Retrieval of monthly rainfall indices from microwave radiometric measurements using probability distribution functions, *J. Atmos. Oceanic Technol.*, *8*, 118–136.

Wilheit, T. T., C. D. Kummerow, and R. Ferraro (2003), Rainfall algorithms for AMSR-E, *IEEE Trans. Geosci. Remote Sens.*, *41*, 204–214.

Wilks, D. S. (1995), *Statistical Methods in the Atmospheric Sciences*, Academic, San Diego.

Wu, R., and J. A. Weinman (1984), Microwave radiances from precipitating clouds containing aspherical ice, combined phase, and liquid hydrometeors, *J. Geophys. Res.*, *89*, 7170–7178.

Zagrodnik, J., and H. Jiang (2013), Investigation of PR and TMI Version 6 and Version 7 rainfall algorithms in landfalling tropical cyclones relative to the NEXRAD stage-IV multi-sensor precipitation estimate dataset, *J. Appl. Meteor. Climatol*, *52*, 2809–2827, doi:http://dx.doi.org/10.1175/JAMC-D-12-0274.1.